ISBN 978-82-326-1024-2 (printed version)
ISBN 978-82-326-1025-9 (electronic version)
ISSN 1503-8181

Doctoral theses at NTNU, 2015:184

Zerihun Kinfe Birhanu

Mathematical Modeling and Simulation of Groundwater Flow and Aquifer Thermal Energy Storage

NTNU
Norwegian University of
Science and Technology
Faculty of Information Technology,
Mathematics and Electrical Engineering
Department of Mathematical Sciences

NTNU – Trondheim
Norwegian University of
Science and Technology

Doctoral theses at NTNU, 2015:184

NTNU

NTNU – Trondheim
Norwegian University of
Science and Technology

Zerihun Kinfe Birhanu

Mathematical Modeling and Simulation of Groundwater Flow and Aquifer Thermal Energy Storage

Thesis for the degree of Philosophiae Doctor

Trondheim, July 2015

Norwegian University of Science and Technology

NTNU – Trondheim
Norwegian University of
Science and Technology

NTNU
Norwegian University of Science and Technology

Thesis for the degree of Philosophiae Doctor

ISBN 978-82-326-1024-2 (printed version)
ISBN 978-82-326-1025-9 (electronic version)
ISSN 1503-8181

Doctoral theses at NTNU, 2015:184

Printed by Skipnes Kommunikasjon as

PREFACE

This thesis is submitted in partial fulfilment of the requirements for the degree of Philosophiae Doctor (PhD) at the Norwegian University of Science and Technology (NTNU). The research is financed by the Norwegian Educational Loan (Quota program) along with the NOMA program, Mathematical and Statistical Modeling (MASTMO), where the latter is administered by Prof. Henning Omre, NTNU, and Dr. Ayele Taye, Hawassa University (HU), Ethiopia.

My supervisors have been Prof. Anne Kværnø (Department of Mathematical Sciences, NTNU), Prof. Harald Krogstad (Department of Mathematical Sciences, NTNU) and Assoc. Prof. Nils-Otto Kitterød (Department of Environmental Sciences, NMBU). The work has been performed at the Norwegian University of Science and Technology.

STRUCTURE OF THESIS

This thesis consists of an introduction and four papers, arranged in a total of five chapters. A brief summary of each papers is given in Section 6 of the introduction.
All four articles involve analysis, implementation and programming aspects. My contribution to these articles has been substantial in all respects.

ACKNOWLEDGMENTS

I wish to express my sincere appreciation to those who have supported me in one way or the other during my stay as a research fellow at NTNU. I would like to acknowledge my Ph.D. supervisors, Prof. Anne Kværnø, Prof. Harald Krogstad and Assoc.Prof. Nils-Otto Kitterød for their tireless commitment and follow-up to see this work come through. I cannot forget their wholehearted support and encouragement right from the start of my Ph.D. career. They have been tremendous mentors for me. I would like to thank them for encouraging my research and for allowing me to grow as a research scientist. Their advice on research as well as my career has been priceless.

I gratefully thank Prof. Henning Omre and Dr. Ayele Taye for financial support under the NOMA-MASTMO project along with the Norwegian Educational Loan Fund (Quota program). Likewise, I thank all administrative staff members of Department of Mathematical Sciences and International Relation office at NTNU who have been kind enough to advise and help in their respective roles. In addition, I would like to thank all the members of the DNA group at NTNU for providing me with a stimulating learning environment. I have made a number of great friends along the way. They have helped me in one way or another in my time as a Ph.D. student at NTNU.

A special thank you goes to Dr.Kevin J. Tuttle, Norconsult, and staff at Avinor, Oslo Airport for inspiring discussions and for providing the data used in this study. I would like to express my appreciation to Dr.Bertil Nistad for his assistance on the COMSOL software.

I am especially grateful to Dr. Tesfa Yigerem, Dr. Maru Alamirew, Dr. Zeytu Gashaw, Dr. Asfafaw Haileselasie and their lovely families that made my time in Trondheim so enjoyable. My warmest thanks go to Abebe E., Berhane

E., Ashenafi L., Tesfaye A. and Kominist A. for their unreserved help during my last period in Trondheim. I have very much enjoyed the friendly environment created by them.

I would like to thank St.George Ethiopian Orthodox Tewhaido church in Trondheim and its members for supporting me to nourish spiritually throughout my study.

Finally, I am greatly indebted to my family, both near and far for their love and never-ending support. Most importantly, none of this would have been possible without my beloved wife, Asne and my lovely son, Nati. Their assistance, understanding and encouragement have made me break through all difficulties and barriers to reach the final success. They form the backbone and origin of my happiness. Their love and support without any complaint or regret has enabled me to complete this Ph.D.

Last but not least, I would like to give honor to the Almighty GOD, through whom everything is possible.

Zerihun Kinfe
Trondheim, July, 2015

CONTENTS

INTRODUCTION

Groundwater is the term used for water in the saturated zone occurring below the ground surface. This water is an important constituent of hydrological cycle and is the major source of water supply in various sectors [19]. During the last decades, the continuously increasing need of water has led to a rapidly growing awareness in the field of groundwater. For groundwater assessment and management it is essential to have a thorough understanding of complex processes viz., physical, chemical and/or biological processes occurring in the groundwater system.

To understand these complexities groundwater models plays an important role. Groundwater models describe the groundwater flow and transport processes using mathematical equations based on certain simplifying assumptions. These assumptions typically involve the dimension of the flow, the geometry of the aquifer, the heterogeneity or anisotropy of sediments or bedrock within the aquifer, boundary and initial conditions. If transport of contaminants are involved, assumptions regarding the contaminant transport mechanisms and chemical reactions are necessary [13]. Because of the simplifying assumptions embedded in the mathematical equations and the many uncertainties in the values of data required by the model, a model must be viewed as an approximation and not an exact duplication of field conditions. Groundwater models, however, even as approximations, are useful investigation tools that groundwater hydrologists may use for a number of applications. Models range from simple two-dimensional analytical groundwater flow models to complex three-dimensional numerical groundwater flow models.

Essentially all natural groundwater flows are three-dimensional. That is, the velocity of a percolating water particle is represented by a vector that has three components. However, there are many situations in which the velocities are nearly coplanar or there is radial symmetry. In these cases, the flow can be analyzed as two-dimensional models with accuracy sufficient for many engineering problems. In some cases the flow problem can be further reduced to a one dimensional problem. The existence of symmetry or special assumptions permits the simplification of many problems. It is important, however, to recognize the size of the errors that such simplifications can entail [5].

1 Groundwater and aquifers

Aquifers

Groundwater is contained in geological formations. If the permeability is high, the geological unit is called an aquifer. The two main types are confined aquifers and unconfined aquifers [8]. If the aquifer is situated between impermeable rocks we call it a confined aquifer. An unconfined aquifer is a layer of water-bearing material without a confining layer at the top of the groundwater, also called the groundwater table, where the pressure is equal to atmospheric pressure. Of that reason an unconfined aquifer is also referred to as phreatic.

Porosity

Porosity is a measure of a medium's ability to store fluid, and is defined as the ratio between the volume of the pores, and the total volume called the bulk volume. Porosity usually is expressed as a percentage of the bulk volume of the material [21]:

$$\text{Effective Porosit}(n) = \frac{\text{Volume of pore space}}{\text{Volume of bulk solid}} \times 100. \tag{1}$$

Sand and gravel may typically be quite porous, whereas solid rock such as granite and other eruptive rocks have usually very low porosity. If water takes up all available pores, we say the formation is saturated. Otherwise, the formation is unsaturated.

Hydraulic conductivity

Hydraulic conductivity is the property of a geological material that relates to its ability to transmit water at a given temperature. This characteristic is also known as the coefficient of permeability [2]. Permeability refers to the case where any fluid moves through a geological material, therefore the term *intrinsic* permeability underlines that this parameter characterizes the soild phase in difference to hydraulic conductivity. Thus, the intrinsic permeability (k) is the ability of geologic material to transmit a fluid, and it is a function of the geological material alone. The relation between intrinsic permeability and hydraulic conductivity can be expressed as $k = \mathbf{K}\mu/\rho_w g$, where μ is dynamic viscosity of the fluid ; ρ_w is water density; $\mathbf{K}$ is the hydraulic conductivity of the porous medium and g is the gravity acceleration [7].

2 The motion of groundwater

The motion of water requires energy. Water can possess several forms of energy. As stated in [5], it possesses potential energy, kinetic energy and pressure energy. Potential energy is the energy that water possesses by virtue of its elevation above the datum level. A mass m_w of water at an elevation z above the datum has a potential energy $m_w g z$. This is the work necessary to move the mass m_w from the datum to the elevation z. The energy that water possesses by virtue of its motion is the kinetic energy. A mass m_w of water that moves with a velocity v has a kinetic energy $\frac{1}{2}m_w v^2$.

If ρ_w is the density of the water, a unit volume of water has a mass ρ_w, a weight $\rho_w g$, and a potential energy $\rho_w g z$. The potential energy per unit weight, that is, the elevation head, is thus $\rho_w g z/\rho_w g = z$. Note that this head has the unit of length. Similarly, the kinetic energy per unit volume is $\frac{1}{2}\rho_w v^2$ and the kinetic energy per unit weight or velocity head is $\frac{1}{2}\rho_w v^2/\rho g = v^2/2g$. The velocity head has the dimension of length. When groundwater is flowing through the pores of the rock or soil formation, the velocity is very small, and the velocity head is usually negligible with respect to the other forms of energy.

The third energy that water possesses is the pressure energy. The pressure of the fluid, p, acting on an area dA produces a force pdA. If the area is displaced by a distance ds in the flow direction, then the force produces an amount of work

$pdAds$ known as flow work. The volume $dAds$ has a weight $\rho_w g dAds$ and the flow work per unit weight is $pdAds/\rho_w g dAds = p/\rho_w g$ known as the pressure head and it has a unit of length.
The sum of the elevation head and the pressure head is known as the piezometric head and given by

$$\phi = z + p/\rho_w g. \tag{2}$$

see [21]. The groundwater head for an elemental volume in an aquifer is the height to which water will rise in a piezometer (or observation well) relative to a consistent datum. Groundwater flows from a higher to a lower head (or potential).

Darcy's Law

It was in 1856 that Henry Darcy carried out experiments which led to what we now call Darcy's Law. Darcy learned that the rate of flow through a column of saturated sand is proportional to the difference in the hydraulic head at the ends of the column and is inversely proportional to the length of the column [7, 8, 23]. Combining these observations and writing an equation in differential form gives Darcy's law:

$$\mathbf{q} = -\frac{\rho_w g \mathbf{k}}{\mu} \cdot \nabla \left(\frac{p}{\rho_g} + z \right) = -\mathbf{K} \cdot \nabla \phi \,. \tag{3}$$

Here $\mathbf{q}$ is the specific discharge (referred to as the Darcy velocity) and ϕ is also called piezometric head. The minus sign is necessary because head decreases in the direction of flow.

The calculation of the Darcy velocity ignores the fact that the aquifer cross-section (A) contains both solid material and pores; consequently the Darcy velocity is a volume average, and has in this sense no direct physical meaning. Nevertheless, because of its convenience mathematically, the Darcy velocity is frequently used. An approximation to the actual seepage (or pore water) velocity can be obtained by dividing the Darcy velocity by the effective porosity n.

$$\mathbf{u} = \frac{\mathbf{q}}{n}. \tag{4}$$

Assuming that the solid matrix as well as the water are incompressible, mass conservation combined with Darcy's law leads to the Boussinesq equation for the hydraulic head,

$$\frac{\partial (S\phi)}{\partial t} + \nabla \cdot [-\mathbf{K}\nabla\phi] = Q_f, \tag{5}$$

where S is the specific storage coefficient, Q_f is the water source/sink density and t is the time. For steady state this becomes

$$\nabla \cdot [-\mathbf{K}\nabla\phi] = Q_f, \tag{6}$$

which is simply the well known Poisson equation.

Flow in phreatic aquifers

A phreatic aquifer is an unconfined aquifer where the top boundary (watertable or the phreatic head) has a link through the pores to the surface, implying that the pressure at the water table is equal to the atmospheric pressure. The hydraulic head at the water table is then the actual height relative to a datum. A completely horizontal water head implies no flow. For the groundwater flowing in an unconfined aquifer between two water reservoirs, the hydraulic head near the reservoirs is approximately equal to the surface height of the reservoir, but even if we know the formation between the reservoirs, we do not necessarily know the location of the watertable.

One of the alternative formulations of the groundwater flow equation may be obtained by invoking the Dupuit assumption (or Dupuit-Forcheimer assumption), where it is assumed that heads do not vary in the vertical direction. It gives reasonable result when the region of the unconfined flow is thin and the slope of the free surface is small.

Consider steady flow without recharge in the vertical two-dimensional xz-plane shown in Fig. 1a. The assumptions of steady flow and a horizontal bottom are intended only to simplify the discussion. Under these conditions, the phreatic surface is a streamline. At every point P along this streamline, $p = 0$, and as consequence $\phi = h$. Where h is the elevation of P above the horizontal impervious bottom that serves as a datum level. In the case considered here, $\phi = \phi(x, z)$ and $h = h(x)$. The specific discharge at P, which is in the direction of the tangent to the streamline, is given by Darcy's law

$$q_s = -K\frac{d\phi}{ds} = -K\frac{dh}{ds} = -K\sin\theta, \tag{7}$$

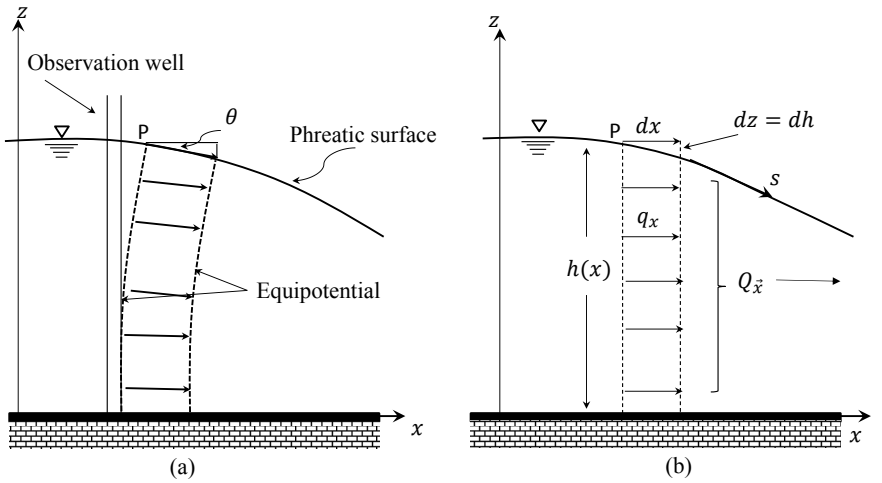

Figure 1: The Dupuit assumption in two dimensional unconfined flow without recharge in the vertical xz-plane, the water table is a streamline

where θ is the angle between the tangent of phreatic surface the horizontal plane (Fig. 1). For small θ, $\sin\theta$ in Eq. 7 can be replaced by the slope, dh/dx and since $\cos\theta \approx 1$,

$$q_x = q_s \cos\theta \approx -K\frac{dh}{dx}.$$

The assumption of small θ is equivalent to assuming that the equipotentials are vertical, i.e $\phi = \phi(x)(= h(x))$, rather than $\phi = \phi(x, z)$, and the flow is essentially horizontal.

For unsteady flow in a three-dimensional domain, the Dupuit assumption presented above is extended to $\phi = \phi(x, y, z, t)$ and $h = h(x, y, t)$. Then, the Dupuit assumption leads to specific discharge expressed by

$$q_x = -K\frac{\partial h}{\partial x}, \quad q_y = -K\frac{\partial h}{\partial y}.$$

Since, by making use of the Dupuit assumption, $\mathbf{q}$ is independent of elevation z, the corresponding total discharge through a vertical surface of unit width (normal to the direction of flow) can be expresses in the vector form:

$$\mathbf{q} = -Kh\nabla h, \quad \text{or} \quad \mathbf{q} = -K\nabla(h^2/2).$$

Recall that the aquifer's bottom is horizontal and serves as a datum level for h.

3 Heat transfer in porous media

The heat transfer equation in porous media is deduced from the principle of energy conservation in the aquifer. Advection of heat is transport by the liquid phase medium, and conduction of heat is transport by the solid phase medium as well as the liquid phase medium. Advective heat flux is passive transport by the moving groundwater:

$$\mathbf{q}_c = (\rho_w c_w T_w)\mathbf{q},$$

where c is the specific heat [9, 11] and the subscripts w and s stand for the liquid phase and solid phase medium, respectively. Using the relation in (4), the advective heat flux is also given by

$$\mathbf{q}_c = n\rho_w c_w T_w \mathbf{u}.$$

In addition to the advective flux, there is a certain amount of diffusive flux in the solid as well as liquid medium. The two diffusive fluxes are given by

$$\mathbf{q}_w = -n\lambda_w \nabla T_w, \qquad \mathbf{q}_s = -(1-n)\lambda_s \nabla T_s,$$

where λ is the heat diffusion coefficient. If the two media are at local thermal equilibrium (when $T_w = T_s = T$), the flux is given by

$$\mathbf{q}_T = -\lambda_m \nabla T,$$

where λ_m is an overall heat diffusion coefficient which is an average between the corresponding values of water and solid:

$$\lambda_m = n\lambda_w + (1-n)\lambda_s$$

see [11, 18]. If a thermally insulated block of aquifer with $T_w \neq T_s$ is left alone, energy conservation implies that the system attains an equilibrium temperature T_m equal to the weighted mean

$$T_m = \frac{\rho_w c_w n}{\rho_m c_m} T_w + \frac{\rho_s c_s (1-n)}{\rho_m c_m} T_s,$$

where

$$\rho_m c_m = (\rho c)_m = \rho_w c_w n + \rho_s c_s (1-n).$$

In respect to conservation laws for solid material and water, since the solid material is stationary, there is no convective heat flux in the solid. For an elemental volume R and no additional heat sources or sinks, the solid's integral heat conservation law reads

$$\frac{d}{dt}\int_R (1-n)\rho_s c_s T_s dV + \int_{\partial R} (1-n)(-\lambda_s \nabla T_s)\cdot \hat{\mathbf{n}} d\sigma = \int_R h(T_w - T_s) dV. \quad (8)$$

Similarly, the integral conservation form for heat in the fluid becomes:

$$\frac{d}{dt}\int_R n\rho_w c_w T_w dV + \int_{\partial R} [n\rho_w c_w T_w \mathbf{u} - n\lambda_w \nabla T_w]\cdot \hat{\mathbf{n}} d\sigma = -\int_R h(T_w - T_s) dV. \quad (9)$$

The differential form of equation 17 and 18 are also expressed as

$$\frac{\partial}{\partial t}(1-n)c_s \rho_s T_s - \nabla\cdot((1-n)\lambda_s \nabla T_s) = h(T_w - T_s), \quad (10)$$

for the heat in the solid and

$$\frac{\partial}{\partial t} n c_w \rho_w T_w + \nabla\cdot(n\rho_w c_w T_w \mathbf{u}_w) - \nabla\cdot(n\lambda_w \nabla T_w) = -h(T_w - T_s), \quad (11)$$

for the transport of heat in the water.

Aquifer Thermal Energy Storage

Thermal energy storage systems around the world are often utilized to provide economical and environmental solutions to the energy problems. Among various types and sizes of storage media, soil or underground aquifers, known as underground thermal energy storage (UTES), are mostly used for seasonal heat/cold storage due to their large thermal capacity and thermal inertia [15]. One of the more common storage type among UTES systems is aquifer thermal energy storage (ATES) system in which groundwater is used to carry the thermal energy into and out of an aquifer [1].

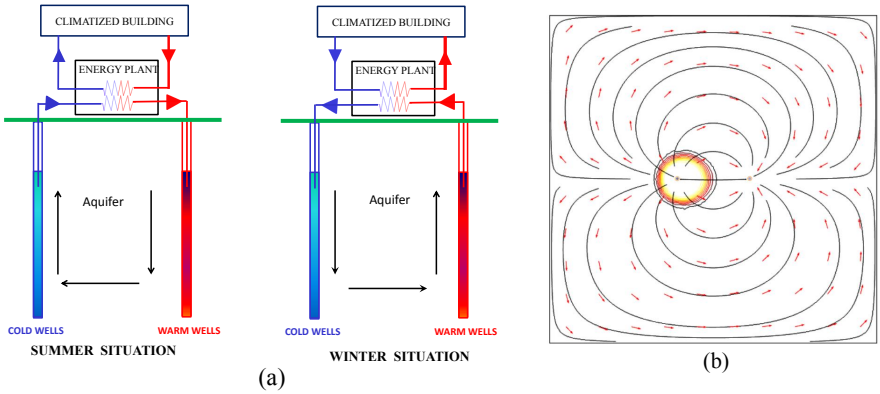

Figure 2: (a) ATES system. (b) The coupled fluid flow and heat transfer. The velocity field (red arrow), stream lines (black lines) and temperature contour (thermal color).

In an ATES system, groundwater is pumped from a supply aquifer for injection or extraction of thermal energy. The groundwater at the changed temperature is then injected back into the same or another aquifer for storage in the aquifer medium (soil or rock). In the opposite season, the stored thermal energy from the aquifer is recovered by pumping out the groundwater, using the stored energy and re-inject the water at a changed temperature back into the aquifer. Of course, to minimize thermal mixing within the aquifer, the supply and injection wells have to be spaced somewhat apart (Fig. 2a). An ATES system usually consists of two or more wells to store warm and/or cold thermal energy in the aquifer, and there are mainly two operating types in the ATES system: cyclic regime and continuous regime . In the cyclic mode, pumping and injection wells are switched by the season, while not switched in the continuous mode [12]. Cyclic flow will create a definite cold and heat reservoir around each well or group of wells. It is possible to maintain a ground volume above or below the natural ground temperature all the time.

The governing partial differential equation of ATES model is given by the fluid flow equation 5 and heat transfer equations 10 and 8. The flow equation and the heat transfer equation are coupled through the fluid velocity $\mathbf{q}$. In most models using Darcy's approximation [24], the flow velocity equation is substi-

tuted into the fluid flow equation and heat transfer equation. The elimination of **q** simplifies the set of the governing equation for thermohydrologyic flow to two equations for pressure and temperature fields. Once these fields are determined, the Darcy velocity **q** or the actual seepage velocity **u** is calculated from the pressure gradient and other parameters. The stream lines, velocity field and the temperature contour of one pumping and one injection wells are shown in Fig. 2b.

The performance of ATES system is defined as the ground thermal load, which is a function of mainly temperature difference between injected and extracted fluids, and fluid flow rate. The performance of the ATES system primarily depends on the thermal interference between warm and cold thermal energy stored in the aquifer [22]. As [12] argued, the borehole distance, the hydraulic conductivity, and the pumping/injection rate affects the thermal interference between two wells.

Oslo airport ATES system

In 1987, the first known ATES system in Norway was established in Seljord. A 10 m deep well was drilled for heating and cooling of Seljord lysfabrikk [14]. However, the largest UTES system in Norway is at Oslo's Gardermoen international airport. This ATES system has been in operation since the airport opened in 1998 and comprises an 8 MW heat pump array, coupled to 18 wells of 45 m depth, 9 for extraction of groundwater and 9 for re-injection. It is located at Gardermoen, one of the largest groundwater reservoirs in Norway. The area consists of glaciofluvial deposits. The soil structure in the area consists of different layers of clay, sand and gravel. The depth to the ground water is 13-14 m, and the storage is located at approximately 20-45 m below surface level [6].

4 Finite element method

In order to analyze a certain system, a mathematical model is developed to describe the system. While developing the mathematical model, some assumptions are made for simplification. Finally, the governing mathematical expression is developed to describe the behavior of the system. The mathematical expression usually consists of differential equations and given conditions.
These differential equations are usually very difficult to obtain solutions which

explain the behavior of the given system. With the advent of high performance computers, it has become possible to solve such differential equations. Various numerical solution techniques have been developed and applied to solve numerous problems in order to find their approximate solutions. Especially, the finite element method has been one of the major numerical solution techniques. One of the major advantages of the finite element method is that a general purpose computer program can be developed easily to analyze various kinds of problems. In particular, any complex shape of problem domain with prescribed conditions can be handled with ease using the finite element method. Good references for descriptions of finite element methods are [3] and [20].
Let us demonstrate the principle of finite element method on the Posisson problem, given by

$$-\Delta u = f \qquad \text{in} \quad \Omega, \tag{12}$$

with boundary conditions

$$\begin{cases} u = g & \text{on} \quad \Gamma_D, \\ \frac{\partial u}{\partial n} = \psi & \text{on} \quad \Gamma_N, \end{cases} \tag{13}$$

where $\Omega \subset \mathbb{R}^d$ is the domain and an open bounded and connected set as shown in Fig. 3, and let $\partial\Omega$ be its boundary.

By multiplying with a test function v, integrating over the domain Ω and applying Green's formula, we get the weak formulation of the problem :

$$\text{Find} \quad u \in W \quad \text{such that} \qquad a(u,v) = F(v), \qquad \forall v \in V \tag{14}$$

where

$$a(u,v) = \int_\Omega \nabla u \nabla v \, d\Omega, \tag{15}$$

$$F(v) = \int_\Omega f v d\Omega + \int_{\Gamma_N} \psi v d\gamma, \tag{16}$$

having

$$V = \{v \in H^1(\Omega) : v|_{\Gamma_D} = 0\}, \tag{17}$$

$$W = \{v \in H^1(\Omega) : v|_{\Gamma_D} = \psi\}. \tag{18}$$

For simplicity we will in the following assume the Dirichlet boundary conditions $g = 0$, so $W = V$. The guarantee for existence and uniqueness of the solution

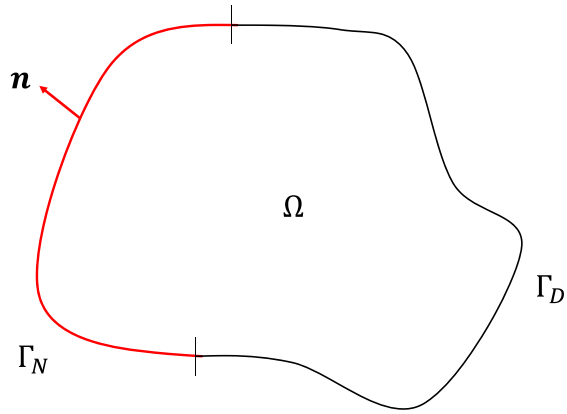

Figure 3: The computational domain Ω

of the variational problem Eq.14 is the Lax-Milgram Theorem which is stated in [20] as

Theorem. ***(Lax-Milgram)*** *Given a Hilbert space V, $a(\cdot,\cdot) : V \times V \to \mathbb{R}$ a continuous, coercive bilinear form, and $F(\cdot) : V \to \mathbb{R}$ a linear and continuous functional. Then, there exists one unique solution to the problem*

$$\textit{Find} \quad u \in V : \quad a(u,v) = F(v), \qquad \forall v \in V. \tag{19}$$

With coercivity, we mean that if there exists a constant $\alpha > 0$ such that

$$a(u,u) \geq \alpha ||u||_V^2 \qquad \forall u \in V.$$

The proof of this is based on two classical results from functional analysis: the Riesz representation theorem, and the Banach closed range theorem. The detail of the proof is found in [3].
The Galerkin approximation method allows us to approximate a continuous problem, such as the weak formulation for the partial differential equation given in into a discrete problem that may be solved numerically. Let V_h be a finite dimensional subspace of V, such that

$$V_h \subset V, \quad \dim V_h = N_h < \infty \quad .$$

The approximate problem takes the form

$$\text{Find} \quad u_h \in V_h : \quad a(u_h, v_h) = F(v_h), \qquad \forall v_h \in V_h, \tag{20}$$

and is called Galerkin problem [20]. Let $V_h = \text{span}\{\varphi_j, j = 1, 2, \ldots, N_h\}$, in which case

$$u_h(\mathbf{x}) = \sum_{j=1}^{N_h} u_j \varphi_j(\mathbf{x}),$$

and Eq. 20 reduces to a system of linear equations:

$$\sum_{j=1}^{N_h} u_j a(\varphi_j, \varphi_i) = F(\varphi_i), \quad i = 1, 2, \ldots, N_h. \tag{21}$$

If we denote the elements $a_{ij} = a(\varphi_j, \varphi_i)$ by a matrix A (called stiffness matrix), the vector with components $f_i = F(\varphi_i)$ by $\mathbf{f}$ and the unknown coefficients u_j by $\mathbf{u}$ Eq. 21 is equivalent to the linear system

$$A\mathbf{u} = \mathbf{f}. \tag{22}$$

Since the Lax-Milgram Theorem holds for any Hilbert space, in particular, for the space V_h and the bilinear form $a(\cdot, \cdot)$ and the functional $F(\cdot)$ are the same as in the variational problem the hypothesis required by the theorem is fulfilled. Thus, the following result applies:

Corollary 1. *The solution of the Galerkin problem Eq. 20 exists and is unique.*

By taking the same hypothesis of the Lax-Milgram Theorem allows to provide the stability result as

Corollary 2. *The Galerkin method is stable, as the following upper bound holds for the solution*

$$||u_h||_V \leq \frac{1}{\alpha} ||F||_{V'},$$

where α is the coercivity constant of the bilinear form $a(\cdot, \cdot)$ and V' is the dual of V, while $||F||_{V'}$ is the norm of the functional F.

The consistency of the method is also stated and proved in [20] by the following Lemma:

Lemma. ***(Céa)*** *The Galerkin method is strongly consistent, that is*

$$a(u - u_h, v_h) = 0 \qquad \forall v_h \in V_h. \tag{23}$$

Based on this lemma one can show that

$$||u - u_h||_V \leq \frac{C}{\alpha} \min_{v \in V_h} ||u - v||_V, \tag{24}$$

where C is the continuity constant and α is the coercivity constant of $a(\cdot, \cdot)$ on V. It is evident that in order for the method to converge, it is sufficient to require that, for N_h tending to infinity, the space V_h tends to fill the entire space V.

Finite Element Spaces

The finite element spaces will consist of piecewise polynomial functions on subdivisions or triangulations $\mathcal{T}_h$ of $\Omega \subset \mathbb{R}^d$,$\mathcal{T}_h = \{K : \text{elements}\}$. For instance if $d = 1$ the elements K will be intervals, if $d = 2$, triangles or quadrilaterals and if $d = 3$ tetrahedrons.

Assume that we have a triangulation $\mathcal{T}_h = \{K : \text{elements}\}$ of $\Omega \in \mathbb{R}^d$, i.e., $\Omega = \cup_{K \in \mathcal{T}_h} K$. The triangulation is admissible if the intersection of two triangles is either empty, or a vertex, or a common side, and from now on, all the triangulations considered are assumed to be admissible. Given a natural number k we associate with $\mathcal{T}_h$ the space X_h of continuous piecewise polynomials of degree k, i.e.,

$$X_h = X_h^k := \{v \in C^0(\Omega) : v|_K \in \mathcal{P}_k, \forall K \in \mathcal{T}_h\},$$

where $\mathcal{P}_k$ denotes the space of polynomials of degree k. Therefore, we can define the finite element approximation $u_h \in X_h$ to the exact solution u as its Galerkin approximation.

5 COMSOL

COMSOL is a finite element analysis and solver software package for various physics and engineering applications, especially coupled phenomena, or multiphysics. It includes a complete environment for modeling any physical phenomenon that can be described using ordinary or PDEs [17]. In addition to conventional physics based user interfaces, COMSOL allows for building coupled systems of PDEs. The PDEs can be entered directly or using the so called weak form. COMSOL also offers an extensive and well managed interface to

MathWorks MATLAB (http://www.mathworks.com/) and its toolboxes for a large variety of programming, preprocessing, and postprocessing possibilities [16].

COMSOL is a well-documented, powerful, and stable tool containing a set of application templates that simulates flow and transport of heat in both saturated and partially saturated heterogeneous porous media. COMSOL can accurately represent complex 3D geological media and structures and their effects on subsurface flow and transport.
COMSOL is also covers a wide range of applications for those interested in integrated hydrological modeling [4]. It is very convenient to have a single modeling platform for simulations of traditional fluid flow problems in addition to heat transport as well as other multiphysics problems. The ability to add user defined functions is a very positive aspect of the software.

6 Summary of Papers

Overview

In this work the groundwater flow model together with the heat transfer in porous media model has been used to investigate the behavior of the ATES system. The location of the water table in unconfined aquifer near a pumping well has been studied using the groundwater flow model. During the study different numerical methods and software have been used.

The papers in this thesis are related to the topic of groundwater flow and heat transfer in porous media. Paper 1 focuses on analytical and numerical solution of radial symmetric aquifer thermal energy storage. The efficiency of the ATES also considered in this paper. Paper 2 considers the effect of regional groundwater flow on the efficiency of ATES for different well orientation. The ATES system of Oslo Airport also studied in this part. Paper 3 is from the preceedings of the ICNAAM-2014 conference and focuses on the effect of boundary condition in the simulation of ATES. Paper 4 considers the location of water table in unconfined aquifer near a pumping well. The numerical result of the full model (in which Darcy's law is directly applied) is compared with the Dupuit- Forchheimer model (vertical flow is ignored).

List of papers

Paper I : Zerihun Birhanu, Nils-Otto Kitterød, Harald Krogstad and Anne Kværnø. *Analytical and Numerical Solutions of Radially Symmetric Aquifer Thermal Energy Storage Problems.* Submitted to Transport in Porous Media.

In this paper we discuss analytical and numerical radial solutions of the differential equations for heat transport in water-saturated porous media. In particular, a similarity solution is obtained for a 2D-horizontal confined aquifer with constant radial flow. Numerical solutions are derived using a high-resolution Lagrangian approach avoiding spurious oscillations and artificial dispersion, and are shown to match the analytical solutions.
The primary purpose of the investigation has been to calculate the recovery factor of an Aquifer Thermal Energy Storage (ATES) system with a cyclic repetition of injection and pumping. Solutions covering both instantaneous and delayed heat transfer between fluid and solid, as well as time varying water flow, are derived and applied to a one-well test case.

In hydrological terms, these solutions should be relevant for a wide range of problems.

Paper II: Zerihun Birhanu, Nils-Otto Kitterød, Harald Krogstad and Anne Kværnø. *Numerical Modeling of Aquifer Thermal Energy Efficiency Under Regional Groundwater Flow, a case study at Oslo Airport.* To appear in Journal of Hydrology Research. Doi: 10.2166/nh.2015.119.

The main purpose of this paper is to present a robust forward model for simulating extraction and storage of thermal energy in an aquifer. The model is a local three dimensional Finite Element Model (FEM) with boundary conditions derived from an analytic large scale model based on the regional water balance. Numerical investigations and thermohydraulic evaluation of a typical dipole injection/extraction system are presented. Most of the simulation results are focused on the spatio-temporal extension of the hot water plume close to the injection well where the main challenges occur with respect to numerical stability. Because the ATES-system is located close to the groundwater divide, the energy recovery is less sensitive to the well configuration with respect to the groundwater flow direction.

Paper III: Zerihun Birhanu, Nils-Otto Kitterød, Harald Krogstad and Anne Kværnø. *Temperature Boundary Conditions for ATES Systems.* AIP Conference Proceedings, 1648, 030032 (2015); doi: 10.1063/1.4912349.

We first briefly recall the mathematical equations needed for the analysis of Aquifer Thermal Energy Storage (ATES) systems. The equations form the basis of a simplified numerical model of (part of) the ATES system located at Oslo Airport, Gardermoen, Norway. This local 3d finite element model consists of an aquifer block penetrated by two wells to form a typical dipole injection-extraction system. Flow boundary conditions are derived from a semi-analytic large scale model. We present here some of the results from the thermohydraulic evaluation of the injection-extraction system, with focus on the effect thermal boundary conditions have on the estimated efficiency of the ATES system.

Paper IV: Zerihun Birhanu and Anne Kværnø. *Numerical Simulation of the Water Table Near a Pumping Well.* Preprint.

In this paper, we study the drawdown of the water table near a pumping well in an unconfined aquifer. Two models for this problems are compared: The Dupuit-Forchheimer model, in which case vertical flow is ignored, thus the model is sufficiently simplified to allow for analytical solutions. This is compared with the solution of a full model, in which Darcy's law has been applied to solve for the hydraulic pressure head, and the water table is the surface for which the hydraulic head equals the atmospheric pressure. A finite element method, utilizing the radial symmetry of the problem, has been implemented to solve this problem.

Bibliography

[1] Andersson, O. (2007). Aquifer thermal energy storage (ATES). In *Thermal energy storage for sustainable Energy Consumption*, pages 155–176. Springer.

[2] Bear, J. (2012). *Hydraulics of groundwater*. Courier Dover Publications.

[3] Brenner, S. C. and Scott, R. (2008). *The mathematical theory of finite element methods*, volume 15. Springer Science & Business Media.

[4] Chui, T. F. M. and Freyberg, D. L. (2007). The use of COMSOL for integrated hydrological modeling. In *Proceedings of the COMSOL Conference 2007 Boston*, pages 217–223.

[5] Delleur, J. W. (2010). *The handbook of groundwater engineering*. CRC press.

[6] Eggen, G. and Vangsnes, G. (2005). Heat pump for district cooling and heating at Oslo airport, Gardermoen. In *Proceedings of the 8th IEA Heat Pump Conference, Las Vegas, Nev*, volume 30.

[7] Haitjema, H. M. (1995). *Analytic element modeling of groundwater flow*. Academic Press.

[8] Hamidi, Y. S. C. A. (1999). Groundwater and surface water pollution. *Groundwater and Surface Water Pollution*.

[9] Hecht-Méndez, J., Molina-Giraldo, N., Blum, P., and Bayer, P. (2010). Evaluating mt3dms for heat transport simulation of closed geothermal systems. *Ground water*, 48(5):741–756.

[10] Johnson, C. (1987). *Numerical solution of partial differential equations by the finite element method*. Cambridge University Press.

[11] Kangas, M. and Lund, P. (1994). Modeling and simulation of aquifer storage energy systems. *Solar energy*, 53(3):237–247.

[12] Kim, J., Lee, Y., Yoon, W. S., Jeon, J. S., Koo, M.-H., and Keehm, Y. (2010). Numerical modeling of aquifer thermal energy storage system. *Energy*, 35(12):4955–4965.

[13] Kumar, C. (2002). Groundwater flow models. *Scientist 'E1'National Institute of Hydrology Roorkee–247667 (Uttaranchal) publication*.

[14] Lee, K. S. (2013). *Underground Thermal Energy Storage*. Springer.

[15] Lee, K. S. and Jeong, S. J. (2008). Numerical modeling on the performance of aquifer thermal energy storage system under cyclic flow regime. *International Journal of Green Energy*, 5(1-2):1–14.

[16] Li, Q., Ito, K., Wu, Z., Lowry, C. S., Loheide, I., and Steven, P. (2009). Comsol multiphysics: A novel approach to ground water modeling. *Groundwater*, 47(4):480–487.

[17] Multiphysics, C. (2012). Comsol multiphysics user guide (version 4.3 a). *COMSOL, AB*.

[18] Nield, D. A. and Bejan, A. (2013). *Convection in Porous Media*. Springer.

[19] Owais, S., Atal, S., and Sreedevi, P. (2008). Governing equations of groundwater flow and aquifer modelling using finite difference method. In *Groundwater Dynamics in Hard Rock Aquifers*, pages 201–218. Springer.

[20] Quarteroni, A. (2010). *Numerical models for differential problems*, volume 2. Springer.

[21] Sterrett, R. J. (2007). *Groundwater and wells*. Johnson Screens.

[22] Yotov, I. (2008). Assessment of natural resources of thermal aquifers—formulation, test data, results. *Geol Balcanica*, 37(1e2):79e84.

[23] Zhang, Y. (2009). Groundwater flow and solute transport modeling. *Draft lecture note on GEOL*, 5030.

[24] Zhang, G. and Koch, M. (1991). The Dupuit assumption and its reliability. Technical report, Technical Report to the Florida Department of Enviromental Protection, Tallahassee, FL.

PAPER 1

ANALYTICAL AND NUMERICAL SOLUTIONS OF RADIALLY SYMMETRIC AQUIFER THERMAL ENERGY STORAGE PROBLEMS

ZERIHUN BIRHANU, NILS-OTTO KITTERØD, HARALD KROGSTAD AND ANNE KVÆRNØ

Submitted to
Transport in Porous Media

ANALYTICAL AND NUMERICAL SOLUTIONS OF RADIALLY SYMMETRIC AQUIFER THERMAL ENERGY STORAGE PROBLEMS

ZERIHUN BIRHANU[1], NILS-OTTO KITTERØD[2], HARALD KROGSTAD[1] AND ANNE KVÆRNØ[1]

[1] *Department of Mathematical Sciences, Norwegian University of Science and Technology, Trondheim, Norway,*
[2] *Department of Environmental Sciences, Norwegian University of Life Sciences, Ås, Norway*

Abstract

The paper discusses analytical and numerical radial solutions of the differential equations for heat transport in water-saturated porous media. In particular, a similarity solution is obtained for a 2D-horizontal confined aquifer with constant radial flow. Numerical solutions are derived using a high-resolution Lagrangian approach avoiding spurious oscillations and artificial dispersion, and are shown to match the analytical solutions.
The primary purpose of the investigation has been to calculate the recovery factor of an Aquifer Thermal Energy Storage (ATES) system with a cyclic repetition of injection and pumping. Solutions covering both instantaneous and delayed heat transfer between fluid and solid, as well as time varying water flow, are derived and applied to a one-well test case. In hydrological terms, these solutions should be relevant for a wide range of problems.

Keywords: Energy transport, Thermal energy, Energy efficency, Heat transfer in porous media, Analytical solution, Lagrangian approach, Similarity solution

1 Introduction

Heat transfer in porous media has received considerable attention and has been the topic of a number of investigations during the last decade [3]. A driving force for research on this subject is engineering applications, such as geothermal

systems [9], heat exchangers [6], thermal insulation [5, 15], and safety issues regarding storage of nuclear waste [25].

In addition to equations for the fluid flow, the mathematical model of heat transfer in porous media is given by second-order partial differential equations for heat energy conservation and flow in the model domain. Two kinds of models can be applied to investigate thermal characteristics of conduction and advection within a porous medium, namely, a thermal equilibrium model and a thermal nonequilibrium model [27]. The difference between the two models is the thermal coupling between the liquid and the solid phase. For the equilibrium model the coupling is modeled as an instantaneous heat transfer. This assumption is close to the reality for homogeneous aquifers with solid particles of minor size (diameter $d_p < 1$ mm). For the non-equilibrium model there is a time delay attached to the heat transfer between the two phases. In the literature of transport in porous media, this model is usually called double porosity model which may also be expanded to a dual permeability model [23].

Researchers have highlighted different analytical and numerical methods to find the solution for this model based on different physical phenomena. In [2] presented the solution of heat transfer in porous media for 1D by using similarity solution method. A two-dimensional numerical model for heat transport in a heterogeneous porous aquifer thermal energy storage system is presented by [10]. They considered transient heat transport phenomenon in a heterogeneous porous aquifer due to hot water injection and validated the solution analytically.

Aquifer Thermal Energy Storage (ATES) is an example of technology where subsurface storage and transport of heat is used to save energy. ATES systems may utilize inter-seasonal heat storage, which means storage of excess energy from summer that is used in winter time for heating purposes. For cooling purposes low temperature water is extracted from cold wells and heated water is injected into hot water wells [5]. Thus, ATES installations actively store cooled and heated groundwater in the ground from respective heating and cooling mode cycles [7]. An ATES system involves both the flow of water and heat transport. In order to predict the performance and efficiency of an ATES system, one possibility is to run detailed numerical simulations, and researchers have long highlighted numerical modelling for analysis and optimization of ATES systems [17]. In some cases, the injection and pumping wells may be simplified to a classical dipole geometry. In this case, the flow field may be simplified to axis symmetry where the flow velocities are governed by the injection/pumping rate

and the aquifer porosity. In the present study, we take advantage of a simplified flow field and solve the transport equation by simple analytical and numerical methods to evaluate the energy efficiency of an idealized ATES system. For fine grained porous media, we calculate and initial energy efficiency about 0.75. This result is close to empirical observations and detailed numerical simulations [4].

Numerical solutions of transport problems are usually affected by artifacts, and because all mathematical models are simplifications of reality, boundary conditions should be specified with great precautions. In [4] showed that the most evident boundary condition of temperature at the top of an unconfined aquifer gave unphysical energy efficiency for simulation experiments of a real ATES system. In this study we use analytical solutions to understand the quality of numerical simulations by doing (simple) numerical experiments. One experiment we carry out is an idealized ATES production sequence by repeating injection and pumping of hot water in a confined aquifer. The performance of the alternative solutions is quantified by a recovery (or efficiency) factor.

2 Mechanisms and Equations

A thermo-hydraulic analysis requires calculation of simultaneous water and heat transport in an aquifer consisting of a solid porous medium (s) with pores filled with water (w). The water flow depends on properties of the water as well as the solid, and the gradient of the hydraulic head, as stated in Darcy's law [19, 20]:

$$\mathbf{q} = -\frac{\rho g \mathbf{k}}{\mu} \nabla \left(\frac{p}{\rho g} + z \right) = -\mathbf{K} \nabla \phi. \tag{1}$$

Here, $\mathbf{q}$ is the specific discharge or the Darcy velocity, $\mathbf{k}$ the intrinsic permeability tensor, z the elevation of the piezometric head relative to a datum level, p the fluid's pressure, ρ water mass density, g the acceleration of gravity, and μ the dynamic viscosity of water. Furthermore, $\mathbf{K} = \rho g \mathbf{k}/\mu$ is the hydraulic conductivity, and $\phi = p/\rho g + z$ is the hydraulic head. The volume average velocity differs from the velocity of the water in the pores, the so-called seepage velocity, $\mathbf{u} = \mathbf{q}/n$, where n is the (effective) porosity [14]. The water density and, more pronounced, viscosity varies with temperature. However, we shall here assume that the flow field represented by $\mathbf{q}$ remains independent of the temperature changes. Assuming that the solid matrix as well as the water are incompress-

ible, mass conservation combined with Darcy's law leads to the Poisson equation for the hydraulic head,

$$\nabla \cdot [-\mathbf{K}\nabla\phi] = Q_w(t), \tag{2}$$

where $Q_w(t)$ is a source/sink term.

The heat energy content per aquifer volume unit may be written

$$\rho_w c_w T_w n + \rho_s c_s T_s (1-n), \tag{3}$$

where c is the specific heat, and subscripts w and s refer to water and solid. At a local temperature equilibrium where, $T_w = T_s = T$, the heat content may be thus expressed as $(\rho c)_m T$, where

$$(\rho c)_m = \rho_w c_w n + \rho_s c_s (1-n), \tag{4}$$

see [13] and [14]. In the following we will use the convention $\rho_m c_m$ for $(\rho c)_m$. The water flow causes advection of heat,

$$\mathbf{q}_c = (\rho_w c_w T_w)\mathbf{q}, \tag{5}$$

whereas conduction/diffusion of heat takes place both in the solid and the liquid,

$$\mathbf{q}_w = -n\lambda_w \nabla T_w, \tag{6}$$

$$\mathbf{q}_s = -(1-n)\lambda_s \nabla T_s, \tag{7}$$

and $\lambda_{w,s}$ are the heat diffusion coefficients. If the two media are at a local thermal equilibrium, the volume average diffusive heat flux may be expressed by

$$\mathbf{q}_T = -\lambda_m \nabla T, \tag{8}$$

where λ_m is a bulk aquifer heat diffusion coefficient,

$$\lambda_m = n\lambda_w + (1-n)\lambda_s, \tag{9}$$

see [14] and [20]. Other expressions for λ_m, e.g. porosity-weighted geometric and harmonic means are also discussed in the literature [20]. In addition, the heterogeneity of the pores induces a certain amount of thermal dispersion, parametrized, in its simplest form as

$$\mathbf{q}_d = \rho_m c_m \hat{\alpha} |\mathbf{q}| \nabla T. \tag{10}$$

Here $\hat{\alpha}$ is the thermal dispersivity length, and the total diffusion flux becomes $\mathbf{q}_T + \mathbf{q}_d$ [1].

If a thermally insulated block of aquifer with $T_w \neq T_s$ is left alone, energy conservation implies that the system attains an equilibrium temperature T_m equal to the weighted mean

$$T_m = \frac{\rho_w c_w n}{\rho_m c_m} T_w + \frac{\rho_s c_s (1-n)}{\rho_m c_m} T_s. \tag{11}$$

How fast this equilibrium is reached depends on the efficiency of the energy exchange between the two media. It turns out to be reasonable to express the heat exchange per time and volume unit as

$$P = h(T_w - T_s), \tag{12}$$

where h is a heat transfer coefficient [16, 20]. The coefficient varies with temperature and the flow, in particular for large flows. Following the discussion in [20], h may be expressed as $h = a_{ws} h_v$, where $a_{ws} = 6\,(1-n)\,/d_p$ is the surface area of the water/solid interface per volume unit, and h_v an expression which for low Reynolds numbers may, for simplicity, be set to

$$h_v = \frac{5\lambda_H}{2d_p}, \;\; \frac{1}{\lambda_H} = \frac{1}{2}\left(\frac{1}{\lambda_w} + \frac{1}{\lambda_s}\right). \tag{13}$$

Here, d_p is the size of the grains making up the solid, and the expression for h becomes

$$h = 15\lambda_H\,(1-n)\,d_p^{-2}. \tag{14}$$

A rough estimate of the time scale Δt towards thermal equilibrium may be obtained from the energy exchange per time unit at the start of the heating, $P = h\,(T_w - T_s)$, compared to the required amount of energy to be transferred, $E = (1-n)\rho_s c_s (T_w - T_s)$:

$$\Delta t = \frac{E}{P} = \frac{1}{15}\frac{\rho_s c_s}{\lambda_H} d_p^2. \tag{15}$$

The time scale is thus only dependent on basic material constants and the grain size. With typical values for rock, we obtain

$$\Delta t\,[\mathrm{s}] \approx 0.15 \times (d_p\,[\mathrm{mm}])^2\,. \tag{16}$$

A similar time scale may actually be derived from the heating of spheres discussed in [11].

For an elemental aquifer volume R with boundary ∂R, the solid's integral conservation law reads

$$\frac{d}{dt}\int_R (1-n)\rho_s c_s T_s dV + \int_{\partial R}(1-n)(-\lambda_s \nabla T_s)\cdot \hat{\mathbf{n}} d\sigma = \int_R h(T_w - T_s)dV. \quad (17)$$

Note that since the solid is stationary, there is no convective heat flux. Similarly, the integral conservation form for heat in the water is

$$\frac{d}{dt}\int_R n\rho_w c_w T_w dV + \int_{\partial R}[\rho c_w T_w \mathbf{q} - n\lambda_w \nabla T_w]\cdot \hat{\mathbf{n}} d\sigma = -\int_R h(T_w - T_s)dV. \quad (18)$$

The differential forms of the conservation laws with the assumptions above become

$$(1-n)\frac{\partial}{\partial t}(\rho_s c_s T_s) - (1-n)\nabla\cdot(\lambda_s \nabla T_s) = h(T_w - T_s), \quad (19)$$

$$n\frac{\partial}{\partial t}(\rho_w c_w T_w) + \nabla\cdot(\rho_w c_w T_w \mathbf{q}) - n\nabla\cdot(\lambda_w \nabla T_w) = -h(T_w - T_s). \quad (20)$$

We observe that when T_w is kept constant and diffusion is neglected, the natural time scale (inverse rate of change) in Eq. 19 is essentially Δt. For d_p less than about a millimetre, the thermal equilibrium is virtually spontaneous and we may assume that T_w and T_s are equal.

For the case where $T = T_w = T_s$, we obtain by adding Eq. 19–20,

$$\frac{d}{dt}\int_R c_m \rho_m T dV + \int_{\partial R}[\rho_w c_w T \mathbf{q} - \lambda_m \nabla T]\cdot \hat{\mathbf{n}} d\sigma = 0, \quad (21)$$

and the corresponding differential form.

$$\frac{\partial(c_m \rho_m T)}{\partial t} + \nabla\cdot(c_w \rho_w T \mathbf{q}) - \nabla\cdot(\lambda_m \nabla T) = 0. \quad (22)$$

If the parameters like c, ρ, λ and the flow $\mathbf{q}$ are assumed to be independent of T, then dividing through with $c_m \rho_m$ in Eq. 22 leads to

$$\frac{\partial T}{\partial t} + \nabla\cdot(\boldsymbol{\kappa} T) - \lambda \nabla^2 T = 0, \qquad \boldsymbol{\kappa} = \frac{\rho_w c_w}{\rho_m c_m}\mathbf{q}, \quad \lambda = \frac{\lambda_m}{\rho_m c_m}. \quad (23)$$

In our model, the flow $\mathbf{q}$ is caused by water injected or pumped with a discharge rate $Q(t)$ from a well located at the origin. When $Q(t) > 0$, water is injected from the well into the aquifer, causing a flow away from the well. During

pumping, $Q(t) < 0$ and the flow is directed towards the well. Utilizing symmetric geometry of the aquifer near the well, the flow is $\mathbf{q} = q_d \mathbf{i}_r$ in which the discharge velocity $q_d = \frac{Q_d}{r^{d-1}}$ where

$$Q_d = \begin{cases} \frac{Q}{HW} & \text{for } d = 1 \text{ (linear flow)}, \\ \frac{Q}{2\pi H} & \text{for } d = 2 \text{ (radial flow)}, \\ \frac{Q}{4\pi} & \text{for } d = 3 \text{ (spherical flow)}. \end{cases} \tag{24}$$

The width W and height H are constants characteristic for the aquifer. In this case, Eq. 23 becomes

$$\frac{\partial T}{\partial t} + \frac{\kappa_d}{r^{d-1}} \frac{\partial T}{\partial r} = \frac{\lambda}{r^{d-1}} \frac{\partial}{\partial r} \left(r^{d-1} \frac{\partial T}{\partial r} \right), \qquad \kappa_d = \frac{\rho_w c_w}{\rho_m c_m} Q_d. \tag{25}$$

Using the same symmetry considerations in the nonequilibrium case Eq.19–20 become

$$\frac{\partial T_s}{\partial t} = \frac{\lambda_s}{\rho_s c_s} \frac{1}{r^{d-1}} \frac{\partial}{\partial r} \left(r^{d-1} \frac{\partial T_s}{\partial r} \right) + \frac{h}{(1-n)\rho_s c_s} (T_w - T_s), \tag{26}$$

$$\frac{\partial T_w}{\partial t} + \frac{Q_d}{n} \frac{1}{r^{d-1}} \frac{\partial T_w}{\partial r} = \frac{\lambda_w}{\rho_w c_w} \frac{1}{r^{d-1}} \frac{\partial}{\partial r} \left(r^{d-1} \frac{\partial T_w}{\partial r} \right) - \frac{h}{n\rho_w c_w} (T_w - T_s). \tag{27}$$

3 Analytical Solutions

We shall consider the formation of a hot water plume in a local thermal equilibrium aquifer generated by a constant hot water source at the origin. Consider Eq. 25 with the following initial and boundary conditions:

$$T(r, 0) = 0, \qquad T(0, t) = 1, \qquad \lim_{t \to \infty} T(r, t) = 0, \qquad r, t > 0. \tag{28}$$

If the diffusion term is negligible, Eq. 25 becomes a simple hyperbolic equation which, for any initial temperature distribution, $T(r, 0) = f(r)$, has the solution $T(r, t) = f\left(r^d - d\kappa_d t\right)$. In particular, for the conditions in Eq. 28, the hyperbolic solution is the moving front $T(r, t) = H_c\left(r^d - d\kappa_d t\right)$ where $H_c(x)$ is the complementary Heaviside function ($= 1$ for $x \leq 0$, $= 0$ for $x > 0$). Since $\rho_w c_w$ is typically about twice as large as $\rho_s c_s$, the ratio $\frac{\rho_w c_w}{\rho_m c_m}$ depends on the porosity n and varies between 1 and 2. The temperature front thus moves significantly faster than the discharge velocity q, but slower than the average seepage velocity, $u = q/n$.

The 1-dimensional case

When $d = 1$ Eq. 25 becomes

$$\frac{\partial T}{\partial t} + \kappa_1 \frac{\partial T}{\partial x} = \lambda \frac{\partial^2 T}{\partial x^2}, \tag{29}$$

where we choose the more standard spatial variable x rather than r. In this case, a well known similarity variable is $\eta = (x - \kappa_1 t)/\sqrt{\lambda t}$, which, inserted into the equation results in

$$2\frac{d^2 T}{d\eta^2} + \eta \frac{dT}{d\eta} = 0, \tag{30}$$

with the general solution $T(\eta) = C_1 \mathrm{erf}(\eta/2) + C_2$. However, no solution from this collection satisfies the boundary condition $T(0, t) = 1$. Nevertheless, the similarity solution of the closely related problem satisfying the initial values $T(x, 0) = H_c(x)$, $x \in \mathbb{R}$ is a good approximation:

$$T(x, t) = \frac{1}{2} \operatorname{erfc}\left(\frac{x - \kappa_1 t}{2\sqrt{\lambda t}}\right). \tag{31}$$

A modification of this solution, satisfying all conditions in Eq. 28 exactly has been derived in [21], see also [2], Eq. 6.4.30:

$$T(x, t) = \frac{1}{2}\left(\operatorname{erfc}\left(\frac{x - \kappa_1 t}{2\sqrt{\lambda t}}\right) + \exp\left(\frac{\kappa_1 x}{\lambda}\right) \operatorname{erfc}\left(\frac{x + \kappa_1 t}{2\sqrt{\lambda t}}\right)\right). \tag{32}$$

The similarity solution Eq. 31 and the exact solution Eq. 32 are presented in Fig. 1 together with the hyperbolic front solution $T(x, t) = H_c(x - \kappa_1 t)$. As expected, the similarity solution in Eq. 31 does not satisfy the boundary conditions at $x = 0$. Still, as λ tends to 0, the solution approaches the hyperbolic front, and Eq. 31 becomes a very good approximation.

The 2-dimensional radial symmetric case

For a 2-dimensional problem, assuming radial symmetry, Eq. 25 becomes

$$\frac{\partial T}{\partial t} + \frac{\kappa_2}{r} \frac{\partial T}{\partial r} = \frac{\lambda}{r} \frac{\partial}{\partial r}\left(r \frac{\partial T}{\partial r}\right), \tag{33}$$

which may be rewritten as

$$\frac{\partial T}{\partial t} + \frac{\kappa_2 - \lambda}{r} \frac{\partial T}{\partial r} = \lambda \frac{\partial^2 T}{\partial r^2}. \tag{34}$$

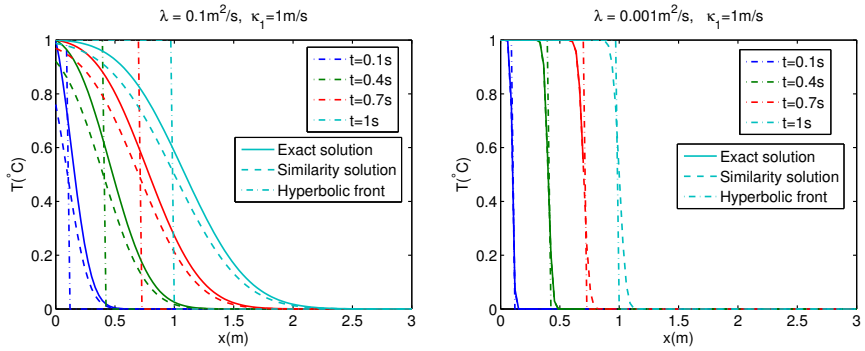

Figure 1: The 1-D similarity solution Eq. 31 and the exact solution Eq. 32 compared with the hyperbolic front for two different values of the diffusion coefficient λ.

Again, it turns out that assuming the similarity variable $\eta = r/\sqrt{\lambda t}$, we obtain an equation

$$\frac{d^2T}{d\eta^2} = \left(\frac{\alpha - 1}{\eta} - \frac{\eta}{2}\right)\frac{dT}{d\eta}, \qquad \alpha = \frac{\kappa_2}{\lambda}, \tag{35}$$

with general solution

$$T(\eta) = C_1 \int_0^{\eta} s^{\alpha-1} e^{-s^2/4} ds + C_2. \tag{36}$$

The solutions may be written in terms of the incomplete Γ-function, defined as

$$\gamma(x, a) = \int_0^x t^{a-1} e^{-t} dt, \qquad \Gamma(a) = \gamma(\infty, a). \tag{37}$$

The radial 2D similarity solution becomes

$$T(\eta) = 1 - \frac{\gamma\left(\frac{\eta^2}{4}, \frac{\alpha}{2}\right)}{\Gamma\left(\frac{\alpha}{2}\right)}, \tag{38}$$

or

$$T(r, t) = 1 - \frac{\gamma\left(\frac{r^2}{4\lambda t}, \frac{\alpha}{2}\right)}{\Gamma\left(\frac{\alpha}{2}\right)}, \tag{39}$$

and the solution is shown is Fig. 2.

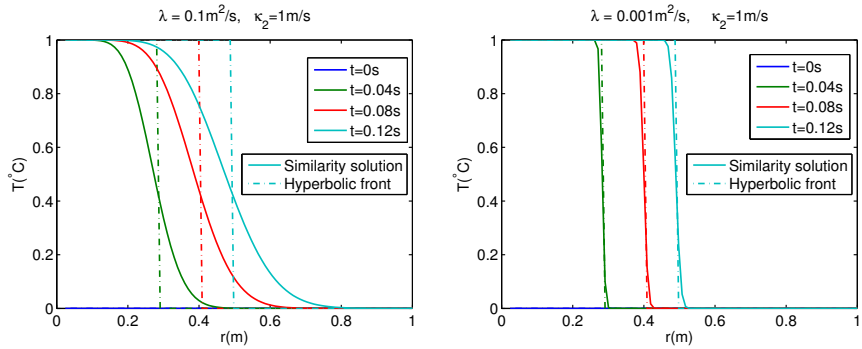

Figure 2: The exact similarity solution Eq. 39 compared with the hyperbolic front for two different values of the diffusion coefficient λ in the 2-dimensional radial symmetric case.

The spherical symmetry 3D-case is easily seen to have intrinsic scales for r and t involving κ_3 and λ, and no simple similarity solution exists. The scaled equation may however be transformed to a 1D heat equation with a space dependent diffusion coefficient [22]. Actually, the numerical algorithm below applies a similar transformation.

4 Computational procedure

We shall now consider a numerical algorithm for solving Eq. 19–20, or the equilibrium model Eq. 23 in the case of symmetric geometry. It turns out that the numerical solution of these problems are nontrivial. They are typically advection dominated, and we have already seen in the previous section that the temperature profile is a sharp front moving away from the source. In the radial and spherical case, the flow becomes very large close to the origin, leading to an almost hyperbolic equation in this region. Advection dominated problems are notoriously difficult to solve numerically. Popular schemes, like central differencing schemes result in unstable or spurious oscillatory solutions. Upwind discretization for the advection term avoid oscillations, but do create artificial diffusion, leading to a smoothed temperature front when applied on a coarse grid. Several other methods have been proposed and discussed in the literature, see e.g. [24] and [18].

We propose a computational procedure utilizing the special structure of the Eq. 25 or Eq. 26–27. The procedure is composed by the well-known Lagrangian approach combined with a coordinate transformation. The idea will first be explained for the equilibrium case Eq. 25.

Before discussing the numerical scheme, it is convenient to say something about the scaling of the problem. Consider a time scale $\mathcal{T}$ for the time t, and $\mathcal{R}$ for the space variable r. A reasonable relation between the two scales is $\mathcal{R}^d = \bar{\kappa}_d \mathcal{T}$, $\mathcal{R}$ is the distance a hyperbolic temperature front moves in time $\mathcal{T}$ for a constant $\kappa_d = \bar{\kappa}_d$. The temperature T will typically be scaled with the temperature of the injected water. With these scales we get the dimensionless equation

$$\frac{\partial T}{\partial t} + v(t)\frac{1}{r^{d-1}}\frac{\partial T}{\partial r} = \frac{\hat{\lambda}}{r^{d-1}}\frac{\partial}{\partial r}\left(r^{d-1}\frac{\partial T}{\partial r}\right) \qquad r > 0, \quad t > 0, \tag{40}$$

where $v(t) = \kappa_d(t)/\bar{\kappa}_d$, $\hat{\lambda} = \lambda\mathcal{T}/\mathcal{R}^2$. As a curiosity, notice that in the case of a constant κ_d, by choosing $\mathcal{R}$ and $\mathcal{T}$ such that $\kappa_d\mathcal{T}/\mathcal{R}^d = \lambda\mathcal{T}/\mathcal{R}^2 = 1$, the parameters are completely absorbed, in the sense that also $\hat{\lambda}$ becomes equal to one. This is possible for $d = 1$ and $d = 3$, but not for $d = 2$. We will not pursue this idea further here.

To handle the singularities in origin in the radial and spherical cases, we introduce the transformation $s = r^d/d$ so that $\partial s = r^{d-1}\partial r$, valid for all dimensions d. In this case, Eq. 40 becomes

$$\frac{\partial T}{\partial t} + v(t)\frac{\partial T}{\partial s} = \frac{\partial}{\partial s}\left(\hat{\lambda}\, a(s)\frac{\partial T}{\partial s}\right), \qquad a(s) = (d \cdot s)^{2(d-1)/d}. \tag{41}$$

Notice that $a(0) = 0$ for the $d \geq 2$, elucidating the hyperbolic nature of the problem close to origin. The numerical difficulties of hyperbolic problems can be resolved by using a Lagrangian method: Given a path $s(t)$ in the (s, t) plane. The solution along this path is $T(s(t), t)$ and the total derivative of T with respect to time becomes

$$\frac{dT}{dt} = \frac{\partial T}{\partial s}\frac{ds}{dt} + \frac{\partial T}{\partial t}, \tag{42}$$

which, inserted into Eq. 41 gives

$$\frac{dT}{dt} + \left(v(t) - \frac{ds}{dt}\right)\frac{\partial T}{\partial s} = \frac{\partial}{\partial s}\left(\hat{\lambda}\, a(s)\frac{\partial T}{\partial s}\right). \tag{43}$$

If we let the path $s(t)$ satisfy $ds/dt = v(t)$, the advection term is eliminated. In fact, the paths $s(t)$ are the characteristics for the hyperbolic equation we obtain

for $\hat{\lambda} = 0$. As a result, Eq. 41 can be solved as a system of differential equations:

$$\begin{aligned} \frac{ds}{dt} &= v(t), \\ \frac{dT}{dt} &= \frac{\partial}{\partial s}\left(\hat{\lambda}\, a(s)\frac{\partial T}{\partial s}\right). \end{aligned}$$

The first equation is an ordinary differential equation, whereas the second one is a just a heat equation with a space dependent diffusion coefficient. This can be discretized in space by some appropriate finite difference schemes, e.g.

$$\frac{ds_i}{dt} = v(t), \tag{44}$$

$$\frac{dT_i}{dt} = \frac{2\hat{\lambda}}{s_{i+1} - s_{i-1}}\left(a_{i+1/2}\frac{T_{i+1} - T_i}{s_{i+1} - s_i} - a_{i-1/2}\frac{T_i - T_{i-1}}{s_i - s_{i-1}}\right), \tag{45}$$

with $a_{i+1/2} = (a(s_{i+1}) + a(s_i))/2$, and initial values $s_i(0) = s_{i,0}$ and $T_i(0) = T(s_{i,0}, 0)$. The procedure is significantly simplified if v is constant, in which case the characteristics $s(t)$ are just straight lines.

The spacial domain can be extended to $\mathbb{R}$ by defining $a(s) = 0$ for $s < 0$. In this case, we may solve Eq. 41 with the boundary conditions:

$$\lim_{s\to-\infty} T(s,t) = 1, \qquad \lim_{s\to\infty} T(s,t) = 0. \tag{46}$$

When water is injected, $v > 0$ and the temperature of the water at the well is $T(0,t) = 1$. This is realized by choosing $T(s,t_0) = T_0(s)$ whenever $s > 0$ and $T(s,t_0) = 1$ for $s \le 0$. Here t_0 is either the initial time or a switching time, that is whenever $v(t)$ changes from negative to positive (from pumping to injection). The procedure is illustrated for the injection phase in Fig. 3.

In order to be able to resolve a sharp front, the characteristics $s_i(t)$ used in the discretization can be concentrated around it.

Example 1. The algorithm described above is used for solving Eq. 40 for $d = 2$, using $\kappa_2 = 1$, $T(0,t) = T_{inj} = 1$ and $T(r,0) = 0$. The exact solution is given by Eq. 39. The problem is first solved by the algorithm described above. The initial computational domain is $(-S_{int}, S_{int}\ )$ where S_{int} is chosen sufficiently large to avoid any influence from the boundaries. The concentration of characteristics around the front is achieved by using

$$\bar{s}_i = -\frac{1}{2} + \frac{i}{N}, \qquad s_i(t_0) = (\mathrm{sgn}(\bar{s}_i))^{p-1}\bar{s}_i^{\,p}\, S_{int}, \qquad i = 0, \cdots, N, \tag{47}$$

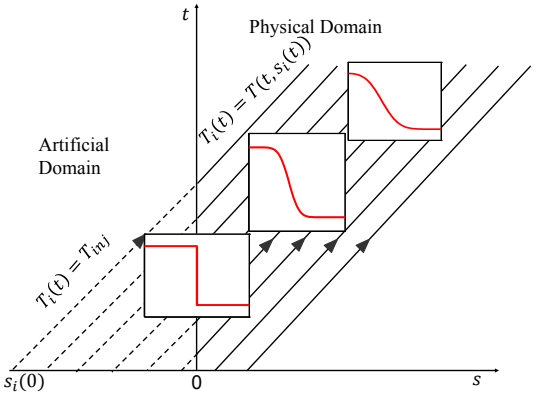

Figure 3: The extended domain and the characteristic lines in the injection phase.

where p is a positive integer, the higher p the stronger concentration. In our experiments, we have used $p = 3$, $N = 100$ and $S_{int} = 2.4$.

For comparisons, the equation Eq. 40 is also solved by a standard difference scheme with constant stepsize. In this case the advection term is approximated with an upwind scheme, $(\partial T/\partial r)(r_i, t) \approx (T_i(t) - T_{i-1}(t))/\Delta r$. For the diffusion term a central difference scheme us applied. The spatial gridsize is $\Delta r = 0.012$.

The problem is solved for different values of $\hat{\lambda}$, and the results are shown in Fig. 2 together with the exact solutions given by Eq. 39. For $\hat{\lambda} = 0.1$, the diffusion is large and the artificial diffusion of the upwind method is insignificant. For smaller values of $\hat{\lambda}$, the front remains sharp, and the effect of the artificial diffusion of the upwind method becomes quite pronounced. The Lagrangian approach preserves the sharp temperature front.

The non-equilibrium case

We now consider the non-equilibrium case Eq. 26–27, which in scaled form becomes

$$\frac{\partial T_s}{\partial t} = \frac{\hat{\lambda}_s}{r^{d-1}} \frac{\partial}{\partial r} \left(r^{d-1} \frac{\partial T_s}{\partial r} \right) + \gamma_s (T_w - T_s), \tag{48}$$

$$\frac{\partial T_w}{\partial t} + v \frac{1}{r^{d-1}} \frac{\partial T_w}{\partial r} = \frac{\hat{\lambda}_w}{r^{d-1}} \frac{\partial}{\partial r} \left(r^{d-1} \frac{\partial T_w}{\partial r} \right) - \gamma_w (T_w - T_s), \tag{49}$$

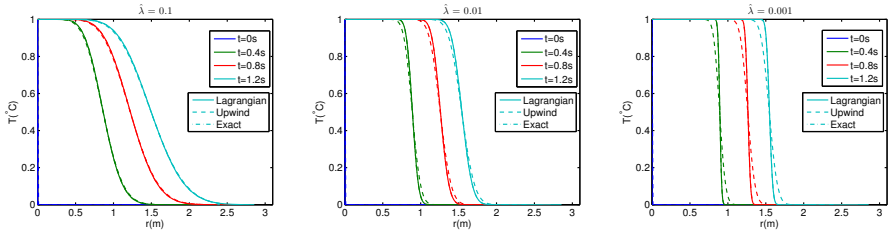

Figure 4: Comparison of the numerical solutions based on the Lagrangian method, and a classical upwind scheme of the 2-dimensional radial symmetric case (Eq. 40) for different values of the diffusion parameter$\hat{\lambda}$. The Lagrangian solution overlaps the exact solution for all three values of $\hat{\lambda}$.

where

$$\hat{\lambda}_s = \frac{\lambda_s}{\rho_s c_s}\frac{\mathcal{T}}{\mathcal{R}^2}, \qquad \hat{\lambda}_w = \frac{\lambda_w}{\rho_w c_w}\frac{\mathcal{T}}{\mathcal{R}^2}, \qquad \gamma_s = \frac{h}{(1-n)\rho_s c_s}\mathcal{T}, \qquad \gamma_w = \frac{h}{n\rho_w c_w}\mathcal{T} \tag{50}$$

and

$$v = \frac{Q_d}{n}\frac{\mathcal{T}}{\mathcal{R}^d}. \tag{51}$$

Again, for a given time scale $\mathcal{T}$ it is appropriate to choose a spatial scale $\mathcal{R}$ such that $v(t)$ is of the size of 1. The boundary conditions in the injection case $(v(t) > 0)$ is

$$T_w(0,t) = T_{inj}, \qquad \frac{\partial T_s}{\partial t}(0,t) = \gamma_s(T_{inj} - T_s(0,t)), \tag{52}$$

(with $T_{inj} = 1$ if the temperature is scaled).

By applying the transformation $s = r^d/d$ and using the Lagrangian approach, we can find the solutions $T_s(s(t),t)$ and $T_w(s(t),t)$ on the characteristics $s(t)$ from

$$\frac{ds}{dt} = v, \tag{53}$$

$$\frac{dT_s}{dt} - v\frac{\partial T_s}{\partial s} = \hat{\lambda}_s\frac{\partial}{\partial s}\left(a(s)\frac{\partial T_s}{\partial s}\right) + \gamma_s(T_w - T_s), \tag{54}$$

$$\frac{dT_w}{dt} = \hat{\lambda}_w\frac{\partial}{\partial s}\left(a(s)\frac{\partial T_w}{\partial s}\right) - \gamma_w(T_w - T_s). \tag{55}$$

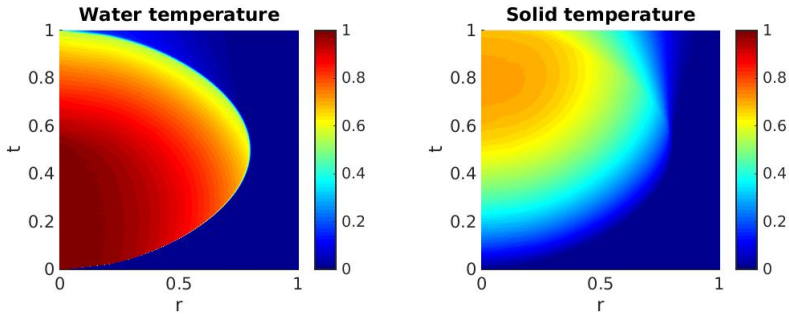

Figure 5: Temperature distribution of water (left) and solid (right) in the aquifer as a function of time t and radial distance r for $v(t) = \cos(\pi t)$. Hot water is injected for $t < 0.5$ and pumped for $t > 0.5$.

However, the advection term is not eliminated as in the equilibrium case, but has moved from the equation of water to the equation of solid, with a sign change. The formulation is still useful, since it is straightforward to construct a spatial grid which is dense around sharp solution profiles, and moves with them. This is illustrated in the following example.

Example 2. Consider the nondimensional equations Eq. 48–49, using $d = 2$ and parameters

$$\hat{\lambda}_w = \hat{\lambda}_s = 10^{-5}, \quad \gamma_w = 1, \quad \gamma_s = 2, \tag{56}$$

and a time dependent flow, $v(t) = \cos(\pi t)$. For $0 < t < 1$, both injection, $0 < t < 0.5$, and pumping, $0.5 < t < 1$, are demonstrated. The equations are solved with the Lagrangian approach, using a central difference approximation for the diffusion terms, and a downwind scheme

$$\frac{\partial T}{\partial s}(s_i, t) \approx \frac{T_{s,i+1} - T_{s,i}}{\Delta s_i} \tag{57}$$

for the advection term. We have used a spatial stepsize Δs_i, varying from $1.1 \cdot 10^{-6}$ to 0.14 and concentrated around the temperature front of the water. The semidiscretized system is solved by MATLABs ODE15s.

The result of the simulation is presented in Fig. 5. We can clearly see how the hot water plume develops with time t. The concentration of characteristics moves with the temperature front, which remains sharp. At the same time, there is a heat exchange from water to solid, and the temperature of the water behind

the front is reduced at the same time as that of the solid increases. The diffusion most of the time is almost negligible, but will cause a slight smoothing of the front. When $t \to 1$, the front approaches the well with increasing velocity, and the smoothing of the front becomes more pronounced. This example illustrates the numerical challenge, namely the coupling of advective and diffusive physics. Usually, the numerical solutions of such problems are suffering from artifacts, such as numerical diffusion and/or oscillations, but in this case it is possible to suppress the numerical artifacts to negligible levels.

5 Case study: Temperature profile near a well in an ATES system

In this section, we consider the temperature propagation around a hot well in an ATES system. The physical and thermal properties of the Gardermoen aquifer where obtained from [12] and [26], and is given in Table 1. The ATES system is typically operating in one of two modi: Injecting hot water during daytime and extracting it during nighttime, resulting in a full operational cycle of 24 hours. Alternatively, the warm water is injected during the summer months, and extracted in the winter, giving a cycle of one year. In reality, a combination of these are used, but in our study, we only consider the first modi, assuming the injection and extraction periods to be of equal lengths, 12 hours.

The Gardermoen aquifer is a delta structure deposited in a glacio-fluvial/glacio-marine environment during the last deglaciation of the Scandinavian crust (approx. 10.000 B.P., [26]). The river discharge and the sediment load from the melting glacier were significant, which explains the wide range of grain sizes of the sediments from boulders ($d_p > 500$mm, at the proximal side of the delta), to fine sand and silt ($d_p <\sim 1$mm) at the distal side of the delta. The ATES system for this case study was located in the delta foresets with homogeneous fine sand, but it is interesting to compare the energy efficiency of this ATES with an alternative locations. We therefore let the sediments vary form $d_p = 1$mm, which correspond to a foreset location, to $d_p = 500$mm mimicking a location close to the glacial portals. In that case, the aquifer permeability would have been better, but to keep the experiment as simple as possible, we let the pumping rate and the porosity be the same for all grain sizes. In Table 2 the value of the heat transfer coefficient h, Eq. 14, and the time scale towards thermal equilibrium Δt, Eq. 16, for different particle size are shown. So we can conclude that within time scales given by the injection/extraction periods, there is

almost thermal equilibrium for realistic particle sizes. It is still of interest to see what happens in the initial injection phase, before thermal equilibrium is established, so we will solve Eq. 26–27. In a horizontal confined aquifer we can assume radial symmetry in the vicinity of a well, so $d = 2$. Initial and boundary conditions for the first injection phase is

$$T_w(0,t) = T_{inj}, \qquad T_w(r,0) = T_0, \tag{58}$$

$$\frac{\partial T_s}{\partial t}|_{r=0} = \gamma_s(T_w - T_s), \qquad T_s(r,0) = T_0. \tag{59}$$

The equations are solved by the numerical approach outlined in Section 4.

Property	**Symbol**	**Value**
Porosity	n	0.1507
Density of fluid	ρ_w	1000 kg/m^3
Density of aquifer	ρ_s	2630 kg/m^3
Specific heat of fluid	c_w	4200 J/kgK
Specific heat of solid	c_s	800 J/kgK
Thermal conductivity of fluid	λ_w	0.6 W/mK
Thermal conductivity of solid	λ_s	2.0 W/mK
Injection/pumping rate	Q	28 m^3/hr
Temperature of the injected water	T_{inj}	30 °C
Aquifer initial temperature	T_0	4 °C
Aquifer height	H_0	24.4 m

Table 1: Physical and thermal properties of fluid and aquifer for the thermo-hydraulic modelling of the Gardermoen aquifer.

d_p	500mm	100mm	10mm	5mm	1mm
h[W/mK]	49.3	1.2×10^3	1.2×10^5	4.9×10^5	1.2×10^7
Δt	10.3 hr	25 min	15 sec	3.8 sec	0.15 sec

Table 2: The heat transfer coefficient (Eq. 14) and the estimated time scale (Eq. 16) towards thermal equilibrium for different particle size.

Transient injection phase

In Fig. 6 we present the temperature profiles for the first few seconds of the injection period. The first rows shows the situation for particle size $d_p = 1$mm.

Thermal equilibrium happens almost immediately in this case, but the energy transfer still has an effect in the sense that the temperature front become more smooth. Also notice that after 0.15 sec, the solid temperature at the wall has reached to about 2/3 of the water temperature, while the water is almost cooled at the front. This is consistent with the fact that $(1-n)\rho_s c_s/(n\rho_w c_w) \approx 2.8$, thus we expect the water to cool down approximately 3 times as fast as the solid heats up. The lower row gives the same profile for $d_p = 5$mm and $d_p = 10$mm, and as expected, the heat exchange is significant slower in these cases. As a consequence, the width of the front increases.

Observe the similarities of the top left and the lower right plots in Fig. 6. This is due to the fact that the thermal transfer coefficient h given by Eq. 14 is proportional to d_p^{-2}. For the 2-dimensional radial symmetry case, the two solutions may be proved to be identical up to scalings of t and r.

Energy efficiency

In this part we study the energy recovery from an ATES well based on 12 hours injection and extraction periods. In general, the energy transfer E in the well over a time interval τ is given by

$$E(\tau) = \int_\tau \rho_w c_w \left(T_{w,0}(t) - T_0\right) Q(t)\, \mathrm{d}t, \tag{60}$$

where $T_{w,0} = T_w(0,t)$ is the water temperature at the well. The efficiency can me measured in terms of the energy recovery factor given by, [8]

$$\theta = \frac{|E(\tau_{extraction})|}{|E(\tau_{injection})|}. \tag{61}$$

Clearly, if the injected water has a constant temperature and the injection rate Q is constant, then $E(\tau_{injection}) = \rho_w c_w (T_{inj} - T_0) Q \tau_{injection}$, however, during pumping the water temperature at the well will vary. The temperature of the water and solid at the well over five consecutive cycles are given in Fig. 7, as well as the recovery rate over these cycles.

We observe that the heat exchange have a significant impact on the efficiency rate for $d_p = 500$mm, otherwise not. We notice that the efficiency recovery rate based on this simplified model corresponds well with the rates achieved for an ATES system in the same aquifer presented in [4].

The temperature profile over one cycle (injection and pumping) is given for the two extreme cases $d_p = 500$mm and $d_p = 1$mm in Fig. 8.

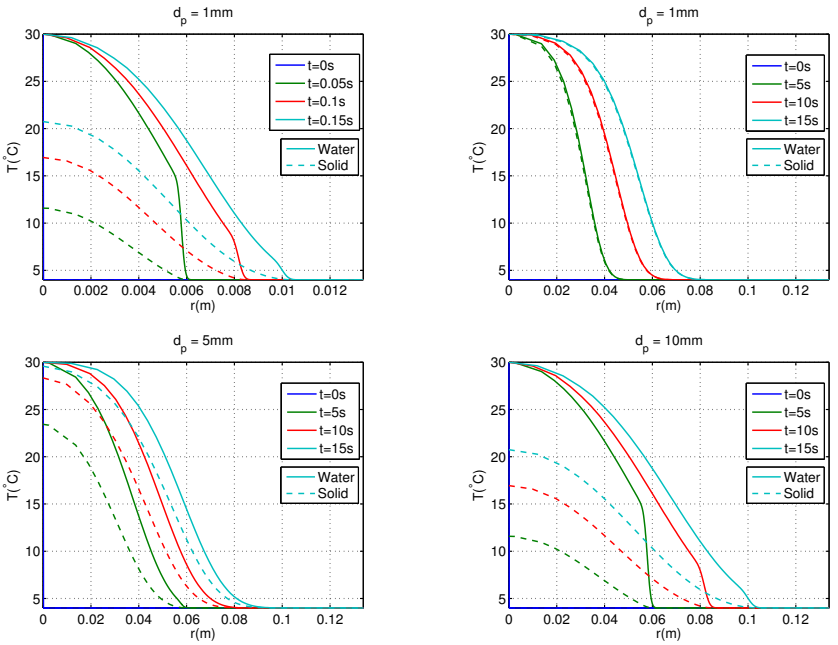

Figure 6: The temperature profile of the solid and the water for different values of d_p[mm] in 2D radial flow near a well. The solid lines indicate the temperature of the water and the broken lines for solid temperature. The upper row emphasize water and solid temperature profile of the same particle size with different timescale while the bottom row emphasize the water and solid temperature profile of different particle size over the same timescale.

6 Conclusion

This paper has briefly reviewed the differential equations for heat transport in water-saturated porous media, and presented numerical and analytical solutions for radially symmetric flow. In particular, a simple similarity solution was obtained for the heat transfer in a 2D horizontal confined aquifer in local fluid/solid thermal equilibrium. For a time varying fluid flow and different fluid and solid temperatures, that is, the non-equilibrium or delayed case, solutions have to be obtained numerically. The numerical algorithms have been based on

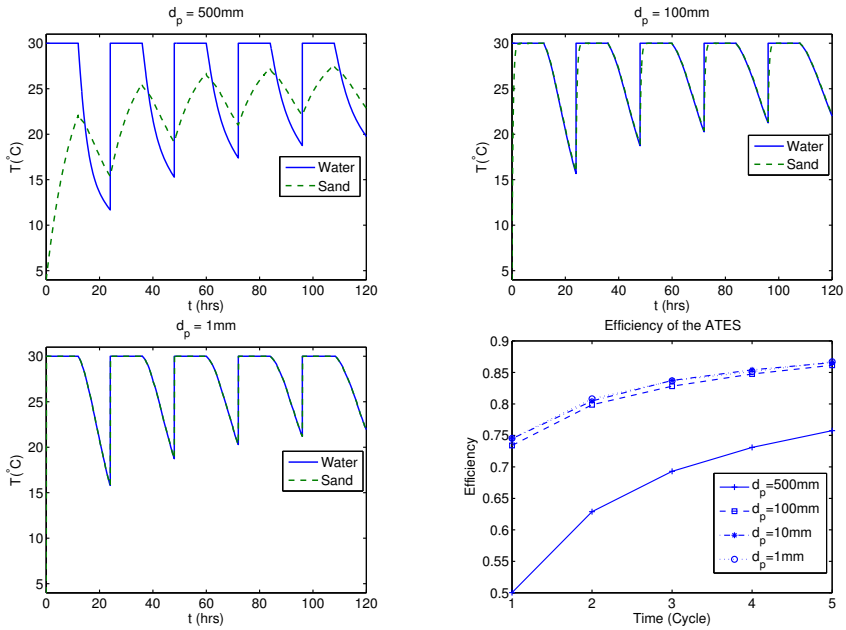

Figure 7: The temperature of the water and solid at the well for five consecutive cycles of 24 hours for aquifers of different particle sizes. In the lower right corner, the corresponding recovery rates.

a semi-discrete Lagrangian formulation for the equilibrium case, and a standard finite difference method for the non-equilibrium case.

The numerical models have enabled us to consider the primary purpose of this investigation, namely to calculate the recovery factor of a one-well ATES system with a cyclic repetition of injection and pumping. It has turned out that the performance is dependent on the total length of the cycle relative to the time scale for the heat transfer between fluid and solid. The latter may be linked to the typical grain size d_p as shown in Table 2. For a total cycle of length 24 hours, referring to Fig. 7, the performance is seen to be virtually independent of the grain size as long as d_p is less than about 100mm ($\Delta t \approx 25$minutes), but significantly affected for $d_s = 500$mm ($\Delta t \approx 10$hours). In the latter case, the efficiency is also significantly reduced.

Based on the presented results, the analytic and numerical solutions should

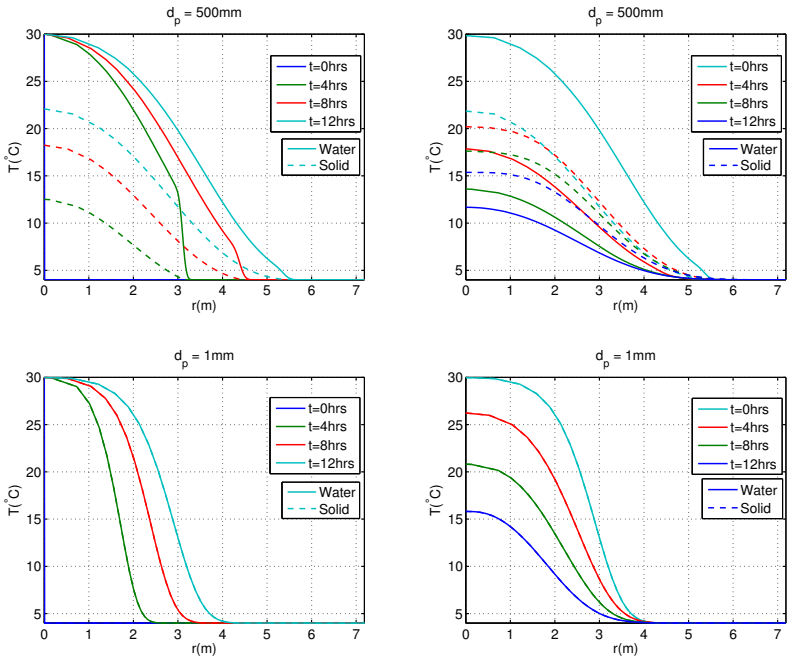

Figure 8: Temperature profiles of water (solid lines) and solid (dashed lines) for different particle sizes The left column shows the temperature profiles during injection, the right during pumping.

provide a consistent tool for the understanding of water and solid temperatures near wells with radial flow.

Bibliography

[1] Bakr, M., van Oostrom, N., Sommer, W.: Efficiency of and interference among multiple aquifer thermal energy storage systems; a Dutch case study. Renewable Energy **60**, 53–62 (2013)

[2] Bear, J., Cheng, A.: Modeling Groundwater Flow and Contaminant Transport, vol. 23. Springer Verlag (2008)

[3] Bejan, A., Kraus, A.D.: Heat Transfer Handbook, vol. 1. John Wiley & Sons (2003)

[4] Birhanu, Z., Kitterød, N.O., Krogstad, H., Kværnø, A.: Temperature boundary conditions for ATES systems (2014). Accepted by AIP Publishing

[5] Birhanu, Z., Kitterød, N.O., Krogstad, H.E., Kværnø, A.: *Numerical Modeling of Aquifer Thermal Energy Efficency Under Regional Groundwater Flow. A case study at Oslo Airport* (2014). Accepted by in Hydrology Research

[6] Diao, N., Li, Q., Fang, Z.: Heat transfer in ground heat exchangers with groundwater advection. International Journal of Thermal Sciences **43**(12), 1203–1211 (2004)

[7] Dickinson, J., Buik, N., Matthews, M., Snijders, A.: Aquifer thermal energy storage: theoretical and operational analysis. Geotechnique **59**(3), 249–260 (2009)

[8] Doughty, C., Hellström, G., Tsang, C.F., Claesson, J.: A dimensionless parameter approach to the thermal behavior of an aquifer thermal energy storage system. Water Resources Research **18**(3), 571–587 (1982)

[9] Ganguly, S., Kumar, M.M.: Analytical solutions for transient temperature distribution in a geothermal reservoir due to cold water injection. Hydrogeology Journal **22**(2), 351–369 (2014)

[10] Ganguly, S., Seetha, N., Kumar, M.M.: Numerical modeling and analytical validation for the movement of thermal front in a hetrogeneous aquifer thermal energy storage system. International Journal of Numerical Analysis And Modeling, Series B **4**, 413–424 (2014)

[11] Gockenbach, M., Schmidtke, K.: Newton's law of heating and the heat equation. Involve, a Journal of Mathematics **2**(4), 419–437 (2009)

[12] Goshu, A., Omre, H.: A posterior inverse model for porosity and hydraulic conductivity in a ground- water aquifer. Ph.D. thesis, Norwegian University of Science, Trondheim (2003)

[13] Hecht-Méndez, J., Molina-Giraldo, N., Blum, P., Bayer, P.: Evaluating mt3dms for heat transport simulation of closed geothermal systems. Ground water **48**(5), 741–756 (2010)

[14] Kangas, M., Lund, P.: Modeling and simulation of aquifer storage energy systems. Solar energy **53**(3), 237–247 (1994)

[15] Kim, J., Lee, Y., Yoon, W., Jeon, J., Koo, M., Keehm, Y.: Numerical modeling of aquifer thermal energy storage system. Energy **35**(12), 4955–4965 (2010)

[16] Kreith, F., Manglik, R., Bohn, M.: Principles of Heat Transfer. Cengage learning (2010)

[17] Lee, K.: Numerical simulation on the continuous operation of an aquifer thermal energy storage system under regional groundwater flow. Energy Sources, Part A: Recovery, Utilization, and Environmental Effects **33**(11), 1018–1027 (2011)

[18] LeVeque, R.J.: Numerical Methods for Conservation Laws, vol. 132. Springer (1992)

[19] Molson, J., Frind, E., Palmer, C.: Thermal energy storage in an unconfined aquifer: 2. model development, validation, and application. Water Resources Research **28**(10), 2857–2867 (1992)

[20] Nield, D.A., Bejan, A.: Convection in Porous Media. Springer (2013)

[21] Ogata, A., Banks, R.B.: A solution of the differential equation of longitudinal dispersion in porous media. Tech. rep., US Government Printing Office Washington, DC (1961)

[22] Philip, J.: Some exact solutions of convection-diffusion and diffusion equations. Water Resources Research **30**(12), 3545–3551 (1994)

[23] Stadler, L., Hinkelmann, R., Helmig, R.: Modeling macroporous soils with a two-phase dual-permeability model. Transport in Porous Media **95**(3), 585–601 (2012)

[24] Strikwerda, J.C.: Finite Difference Schemes and Partial Differential Equations. Siam (2004)

[25] Sun, Y., Buscheck, T., Lee, K., Hao, Y., James, S.: Modeling thermal-hydrologic processes for a heated fractured rock system: impact of a capillary-pressure maximum. Transport in Porous Media **83**(3), 501–523 (2010)

[26] Tuttle, K.: Sedimentological and hydrogeological characterisation of a raised ice-contact delta – the preboreal delta-complex at Gardermoen, southeastern Norway. Ph.D. thesis, University of Oslo. Oslo, Norway (1997)

[27] Yang, C., Kuwahara, F., Liu, W., Nakayama, A.: Thermal non-equilibrium forced convective flow in an annulus filled with a porous medium. The Open Transport Phenomena Journal **3**, 31–39 (2011)

PAPER 2

NUMERICAL MODELING OF AQUIFER THERMAL ENERGY EFFICIENCY UNDER REGIONAL GROUNDWATER FLOW, A CASE STUDY AT OSLO AIRPORT

ZERIHUN BIRHANU, NILS-OTTO KITTERØD, HARALD KROGSTAD AND ANNE KVÆRNØ

To appear in
Journal of Hydrology Research.
Doi: 10.2166/nh.2015.119

Is not included due to copyright

PAPER 3

TEMPERATURE BOUNDARY CONDITIONS FOR ATES SYSTEMS

ZERIHUN BIRHANU, NILS-OTTO KITTERØD, HARALD KROGSTAD AND ANNE KVÆRNØ

Published in
AIP Conference Proceedings,
1648, 030032 (2015); doi: 10.1063/1.4912349

TEMPERATURE BOUNDARY CONDITIONS FOR ATES SYSTEMS

ZERIHUN BIRHANU[1], NILS-OTTO KITTERØD[2], HARALD KROGSTAD[1] AND ANNE KVÆRNØ[1]

[1] *Department of Mathematical Sciences, Norwegian University of Science and Technology, Trondheim, Norway,*
[2] *Department of Environmental Sciences, Norwegian University of Life Sciences, Ås, Norway*

Abstract

We first briefly recall the mathematical equations needed for the analysis of Aquifer Thermal Energy Storage (ATES) systems. The equations form the basis of a simplified numerical model of (part of) the ATES system located at Oslo Airport, Gardermoen, Norway. This local 3d finite element model consists of an aquifer block penetrated by two wells to form a typical dipole injection-extraction system. Flow boundary conditions are derived from a semi-analytic large scale model. We present here some of the results from the thermohydraulic evaluation of the injection-extraction system, with focus on the effect thermal boundary conditions have on the estimated efficiency of the ATES syste.

Keywords: Efficency, Numerical modeling, Natural flow conditions, Thermal energy

1 Introduction

Energy conservation is becoming an increasingly important aspect of essentially all types of economic activity. One method of energy conservation is the Aquifer Thermal Energy Storage (ATES) system utilizing inter-seasonal heat storage. This involves storage of excess energy from summer for use in winter heating applications, and the storage of cooling potential from winter for free cooling in summer. For typical summer conditions, low temperature water from a cold well is pumped through a heat exchanger and used for cooling. This increases

the temperature of the production water before injecting it into a hot well. In winter, the process is reversed. Warm water is pumped from the hot well and sent through the heating system to pre-heat the buildings' air intake. In transferring thermal energy to the air, water becomes cooler, and this cooler water is returned to the cold well. Oslo Airport, located on top of the Gardermoen aquifer in southern Norway, has been operating an ATES system consisting nine cold and hot well pairs attached to an energy plant since the airport opened in 1998. The seasonal operation of the system is illustrated in Fig. 1.

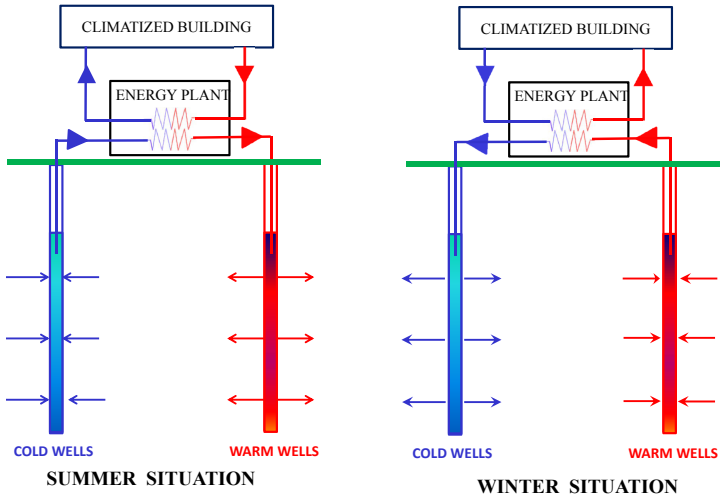

Figure 1: Principal ATES configuration.

In order to predict the performance and efficiency of an ATES system, one possibility is to run detailed numerical simulations, and researchers have long highlighted numerical modeling for analysis and optimization of ATES systems. Numerical models available to simulate an ATES system by modeling the mass and heat transport in the aquifer have been reviewed in [4]. In particular, numerical simulation of the continuous operation of an ATES under regional groundwater flow was carried out by [5], emphasizing the influence of regional groundwater flow on the performance of the system under various operational scenarios. Numerical simulations which describe the efficiency of the ATES sys-

tem at Oslo Airport under regional groundwater flow with thermal insulation of the aquifer have been studied in [1]. In the present work, we address some unresolved problems from the former study. In particular, the effect of boundary conditions on the simulated efficiency of the system is discussed. For the simulation of the ATES system we have applied the commercial finite element software COMSOL Multiphysics [7].

2 Mathematical Model

The thermo-hydraulic analysis requires calculation of groundwater and heat transport in an aquifer consisting of a solid porous matrix (s) with pores saturated with water (w). The flows are governed by a set of coupled partial differential equations describing the mass and heat energy balance. The flow of water depends on properties of the water and the matrix, and the gradient of the hydraulic head, as represented by Darcy's law for groundwater flow [6]:

$$\mathbf{q} = -\frac{\rho g \mathbf{k}}{\mu} \nabla \left(\frac{p}{\rho g} + z \right). \tag{1}$$

Here, $\mathbf{q}$ is the specific discharge or the Darcy velocity, $\mathbf{k}$ the intrinsic permeability tensor, z the elevation of the piezometric head relative to a datum level, p the fluid's pressure, ρ water mass density, g the acceleration of gravity, μ the dynamic viscosity of water, and $\phi = p/\rho g + z$ is the hydraulic head.

We assume that the thermal coupling between the solid and fluid is very good, implying that their respective temperatures are the same. With these assumptions, the energy conservation may be written [8]:

$$\frac{\partial \rho_m c_m T}{\partial t} + \nabla \cdot (c_w \rho_w T \mathbf{q}) + \nabla \cdot [-\lambda_h \nabla T] = \tilde{H}, \tag{2}$$

where c is the specific heat, λ_h is the thermal conductivity, and $\tilde{H}$ is any heat source/sink. The aquifer's heat capacity, depending on the porosity n, is

$$\rho_m c_m = n \rho_w c_w + (1 - n)\, \rho_s c_s, \tag{3}$$

and $c_w \rho_w T \mathbf{q}$ is the advective heat flux [8]. The heat conductivity λ_h has contributions both from molecular diffusion, often expressed as $\lambda_m = n\lambda_w + (1 - n)\, \lambda_s$,

and mechanical dispersion, which may be expressed as $\rho_m c_m \alpha |\mathbf{q}|$, where α is the dispersivity length.

The efficiency analysis of the ATES system in this study is based on a full operational cycle consisting of two periods; injection of hot water followed by extraction of hot water. In general, the energy transfer E in the well over a time interval τ may be written as

$$E(\tau) = \int_{\tau} c_w \rho_w (T(t) - T_0) Q(t) \, \mathrm{d}t, \tag{4}$$

where T is the water temperature at the well, T_0 the ambient groundwater temperature, and Q (m^3/s) the water injection or extraction rate. The energy recovery may then be expressed as the ratio

$$\theta = \frac{E(\tau_{extr.})}{E(\tau_{inj.})}. \tag{5}$$

Model Setup

Oslo Airport is located at Gardermoen, on the largest precipitation-fed aquifer of mainland Norway. A local domain of the aquifer, close to a regional groundwater divide, is utilized as a source for heating and cooling of the indoor space at the airport. The ATES system consists of 18 wells, 9 warm and 9 cold, each with a diameter of 450 mm and drilled down to 45 m below the surface. In order to demonstrate the essential physics, we have decided to simplify the simulations to a pure dipole system with one injection and one extraction well. Pumping and injection volumes are chosen close to the real production volumes. Initial physical parameters for the Gardermoen aquifer were obtained from [2] and [9]. Boundary conditions are derived from an analytic large scale model [3] and are consistent with the regional water balance.

3 Discussion

Figure 2 demonstrates the development of the hot water plume around the warm well for a cycle of 6 months of injection followed by 6 months of pumping. Two different thermal boundary conditions are imposed. The figure to the left shows the temperature propagation for a non insulated aquifer for which

the temperature is constant (4°) at the top and the bottom of the aquifer. The water is rapidly cooled, the hot water plume is quite small, and during the pumping period (bottom row), cold water almost immediately enters the screen, resulting in a simulated recovery factor of about 0.24, far below realistic values at the Gardermoen ATES system. We also observe that almost no hot water is left after one period. As a consequence, subsequent cycles will behave similar.

The same simulations were done on an thermally insulated aquifer, where no thermal flux were allowed at the top and the bottom of the aquifer. The result is given in the right of Fig. 2. In this case, we can see that there are almost no heat loss. We also observe that there is a small plume of hot water left after one period, mostly due to thermal diffusion. After one cycle, the estimated recovery factor is about 0.75. The minor drifting of the temperature plume downwards and to the right of Fig. 2 was due to infiltration of water at top of the aquifer and outflow of groundwater to the right of the model.

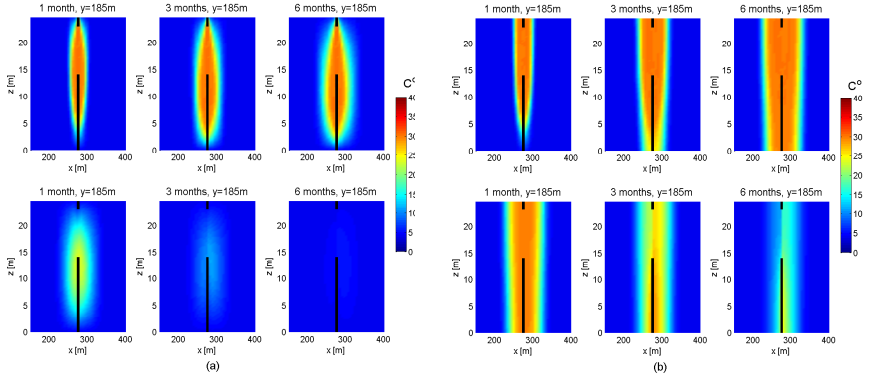

Figure 2: Temperature distributions for a vertical slice at $y = 185$m after warm water injection during the first six months (upper row) and pumping of hot water for another six months (lower row). The vertical broken black line in the top three figures shows the open screen. (a) Thermally non insulated aquifer (constant temperature boundaries). (b) Thermally insulated aquifer (no heat flow across boundaries).

The simulations were also performed over for a period of 5 injection/pumping cycles. The recovery factor has been estimated at the end of each cycle of one year. In the non insulated case, the recovery factor is almost the same over time,

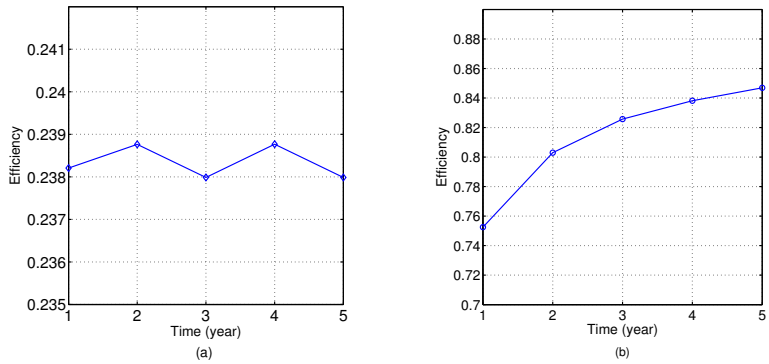

Figure 3: Efficiency of the ATES at Oslo Airport for different temperature boundary condition at the top and bottom of the model. (a) Thermally open aquifer (b) Thermally insulated aquifer condition. For a thermally open aquifer the recovery factor does not increase above 0.239 due to external cooling. For a perfect thermally insulated aquifer the recovery factor increases due to a better containment of the escaped hot water.

due to the fact that during one period, all hot water has either been pumped, or cooled down from the top/bottom boundaries. In the insulated case, the recovery factor increases over time. This because the small plume of hot water left after the first cycle will be recovered in the next one. This is far closer to realistic values.

This initial study indicates that the assumption of a thermal insulated aquifer gives better estimates for the recovery rate that the non-isolated one. These are both extreme cases, the truth is probably somewhere between. To get an accurate picture of the hot water transport in the subsurface there are also other effects that could have been considered. One is the drawdown near the pumping wells, and a different issue is the of temperature dependent viscosity of water. This is left for future work.

4 Conclusion

This paper has briefly recalled the differential equation for modeling and assessment of aquifer thermal energy storage systems. Numerical simulations have

been carried out to see the thermal behavior of an ATES system with two wells. The simulation results clearly indicate the thermal boundary conditions may have a significant effect on the estimated efficiency of the ATES system.

Bibliography

[1] Birhanu, Z., Kitterød, N. O., Krogstad, H. E., and Kværnø, A. (2014). *Numerical Modeling of Aquifer Thermal Energy Efficency Under Regional Groundwater Flow. A case study at Oslo Airport.* Submitted to Hydrology Research.

[2] Goshu, A. and Omre, H. (2003). *A posterior Inverse model for porosity and hydraulic Conductivity in a ground- water aquifer.* PhD thesis, Trondheim.

[3] Kitterød, N-O. (2004). Dupuit-forchheimer solutions for radial flow with linearly varying hydraulic conductivity or thickness of aquifer. *Water Resources Research*, 40(11):W11507.

[4] Lee, K. S. (2010). A review on concepts, applications, and models of aquifer thermal energy storage systems. *Energies*, 3(6):1320–1334.

[5] Lee, K. S. (2011). Numerical simulation on the continuous operation of an aquifer thermal energy storage system under regional groundwater flow. *Energy Sources, Part A: Recovery, Utilization, and Environmental Effects*, 33(11):1018–1027.

[6] Molson, J., Frind, E., and Palmer, C. (1992). Thermal energy storage in an unconfined aquifer: 2. model development, validation, and application. *Water Resources Research*, 28(10):2857–2867.

[7] Multiphysics, C. (2012). Comsol multiphysics user guide (version 4.3 a). *COMSOL, AB.*

[8] Nield, D. A. and Bejan, A. (2013). *Convection in Porous Media.* Springer.

[9] Tuttle, K. (1997). *Sedimentological and Hydrogeological Characterisation of a Raised Icecontact delta-the Preboreal Delta-Complex at Gardermoen, Southeastern Norway.* PhD thesis.

PAPER 4

NUMERICAL SIMULATION OF THE WATER TABLE NEAR A PUMPING WELL

ZERIHUN BIRHANU AND ANNE KVÆRNØ

Preprint

NUMERICAL SIMULATION OF THE WATER TABLE NEAR A PUMPING WELL

ZERIHUN BIRHANU[1] AND ANNE KVÆRNØ[1]

[1] *Department of Mathematical Sciences,*
Norwegian University of Science and Technology,
Trondheim, Norway

Abstract

In this paper, we study the drawdown of the water table near a pumping well in an unconfined aquifer. Two models for this problems are compared: The Dupuit-Forchheimer model, in which case vertical flow is ignored, thus the model is sufficiently simplified to allow for analytical solutions. This is compared with the solution of a full model, in which Darcy's law has been applied to solve for the hydraulic pressure head, and the water table is the surface for which the hydraulic head equals the atmospheric pressure. A finite element method, utilizing the radial symmetry of the problem, has been implemented to solve this problem.

1 Introduction

Groundwater hydrologists distinguish between two basic types of flow: confined flow and unconfined flow [4]. Confined flow occurs in an aquifer which is sandwiched between two "impermeable" geological formations, e.g., a layer of saturated sand and gravel between two clay layers. Unconfined aquifers, in contrast, have as their upper aquifer boundary the water table, whose position depends on the groundwater flow regime and is a priori not known [9].

Many researchers utilized several methods to determine the location of the water table boundary. Several examples of analytical solutions for steady state piezometric heads in phreatic and confined aquifers with radial symmetric flow was carried out in [1]. In [2] performed the method of fundamental solutions in order to determine the free boundary in saturated seepage problems. Similar, [5] has utilized axial symmetry of delta structures. These analytical solutions can be obtained by introducing the Dupuit-Forchheimer assumptions, the vertical component of the flow is ignored. But, [3] proved that the Dupuit-Forchheimer

approach sometimes may be inadequate in terms of characterizing groundwater flow in an unconfined aquifer. In order to overcome this problem several numerical solutions and techniques have been introduced.

Our intention with this work is to make a preliminary study of the water flow during pumping close to a well in an unconfined aquifer. Usually the water table in this case is found by the use of the Dupuit-Forchheimer assumption. However, this can not be true very close to the well. In the present work, we apply a simple finite element method to solve the full problem, and we compare the water table and hydraulic head found by this strategy with this of the Dupuit approximation.

2 Mathematical model

The rate of flow of water through a porous medium is related to the properties of the water, the properties of the porous medium, and the gradient of the hydraulic head, as stated by Darcy's law [1, 7]:

$$\mathbf{q} = -\frac{\rho g \mathbf{k}}{\mu} \nabla \left(\frac{p}{\rho g} + z \right) = -\mathbf{K} \nabla \phi. \tag{1}$$

Here $\mathbf{q}$ is the specific discharge or the Darcy velocity, $\mathbf{k}$ the intrinsic permeability tensor, z the elevation of the piezometric head relative to datum level, p the fluid's pressure, ρ water mass density, g the acceleration of gravity, and μ the dynamic viscosity of water. Furthermore $\mathbf{K} = \rho g \mathbf{k}/\mu$ is the hydraulic conductivity and $\phi = p/\rho g + z$ is the hydraulic head. Conservation of mass for water combined with Darcy's law result in the continuity equation for steady fluid flow in the medium,

$$\nabla \cdot [-\mathbf{K} \nabla \phi] = Q_f, \tag{2}$$

where Q_f is water source /sink density. In the present work, we assume there are no internal sinks or sources. Moreover, we will assume the aquifer to be homogeneous and isotropic, thus K has a constant scalar value.

Consider the radial symmetric flow of water for the geometry described in Fig. 1. The flow domain is sufficiently large such that the effect of the pumping is negligible at $r = R$, so at this boundary we set $\phi = H_0$, that is the head (and the height of the water table) in the undisturbed case. The height of the water

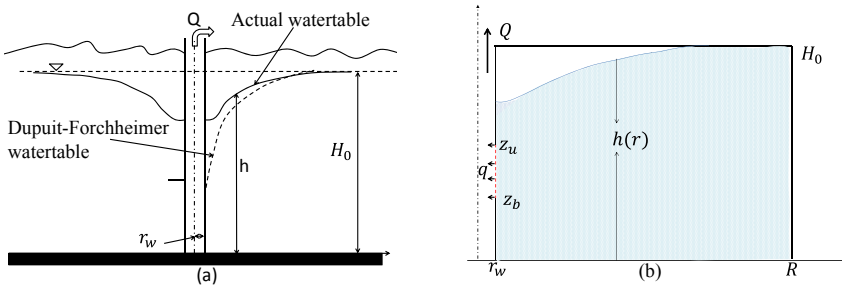

Figure 1: The radial flow to a well in unconfined aquifer

table, $h(r)$ measured from the datum level at $z = 0$, the bottom of the aquifer. The bottom layer is given to be impermeable and we assume there is no infiltration through the top boundary. At a free water surface, the pressure component of the total head is zero; hence the hydraulic head at the water's surface is equal to the elevation component of this surface at a given point: $h = \phi$. The radius of the well is r_w and water is pumped out from the well with rate Q through the screen located between z_b and z_u (see Fig. 1b). The pumping well cause a drawdown of the water table near the well. Thus the flow domain Ω becomes $r_w \leq r \leq R, 0 \leq z \leq h(r)$, where $h(r)$ depends on Q. Our aim is to find this domain.

A method first developed by Dupuit in 1863, and improved by Forchheimer in 1930, were used to find solutions to problems of flow to parallel canals and to pumped wells, [4]. In the derivation Dupuit and Forchheimer assumed the flow pattern to be steady and horizontal, thus neglected the variation of the piezometric head with depth ($\partial\phi/\partial z = 0$) meaning that the head along any vertical line is constant, [6]. Physically, this assumption is not true. The actual and Dupuit's assumption groundwater flow patterns are shown in Fig. 2. But, under the assumptions of Dupuit and Forchheimer, the discharge of water is proportional to h, thus

$$\bar{\mathbf{q}} = h \cdot \mathbf{q} = -K \cdot h \cdot \nabla h = -\frac{1}{2} K \cdot \nabla h^2, \tag{3}$$

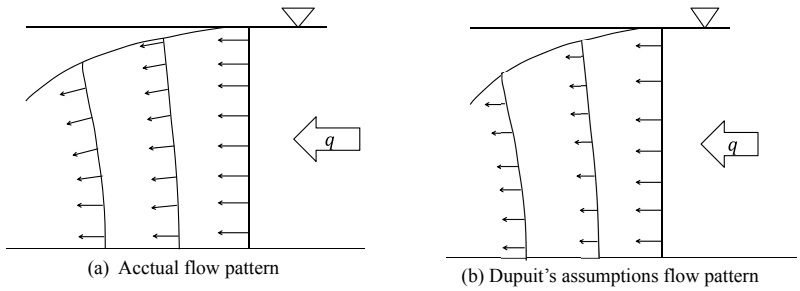

(a) Acctual flow pattern (b) Dupuit's assumptions flow pattern

Figure 2: Actual and Dupuit assumption groundwater flow pattern

and the total pumping rate becomes

$$Q = -2\pi r h \cdot \bar{q} = \pi r K \nabla h^2 = \pi r K \frac{dh^2}{dr}. \tag{4}$$

Integrating Eq. 4 and using the boundary condition $h = H_0$ at $r = R$, we obtain

$$h^2(r) = H_0^2 - \frac{Q}{\pi K} \ln\left(R/r\right), \tag{5}$$

see [1]. The dashed curve in Fig. 1 gives the unconfined surface elevations $h = h(r)$, as expressed by Eq. 5. At the well, the height is

$$h_w^2 = H_0^2 - \frac{Q}{\pi K} ln(R/r_w). \tag{6}$$

Clearly, for large pumping rates or small well radiuses, this becomes completely unphysical.

The full problem

For the aforementioned flow conditions, the steady state flow equation without any internal source in an homogenous aquifer is given by the Laplace equation (see Eq. 2):

$$\Delta\phi = 0 \quad \text{on} \quad \Omega = \{r, z : 0 < z < h(r), r_w \leq r \leq R\}, \tag{7}$$

which by exploiting the radial symmetry becomes

$$\left(\frac{1}{r}\frac{\partial}{\partial r}\left(r\frac{\partial \phi}{\partial r}\right)+\frac{\partial^2 \phi}{\partial z^2}\right)=0. \tag{8}$$

The boundary conditions are given by

$$\phi(R,z)=H_0, \qquad 0\leq z\leq H_0. \tag{9}$$

At the well $r=r_w$ we have

$$\frac{\partial \phi}{\partial r}=\begin{cases}-q & z_b\leq z\leq z_u,\\ 0 & \text{otherwise,}\end{cases} \tag{10}$$

where the flux is $q=Q/(2\pi r_w(z_u-z_b))$. The base is impervious, thus

$$\frac{\partial \phi}{\partial z}=0, \qquad z=0, \qquad r_w\leq r\leq R, \tag{11}$$

and, since we assume no infiltration throughout the upper surface

$$\frac{\partial \phi}{\partial n}=0, \qquad z=h(r), \qquad r_w\leq r\leq R, \tag{12}$$

where n denotes the normal to the surface and $h(r)$ is the height of the water table. Finally the phreatic surface is given by $p=0$, which becomes

$$\phi(r,h(r))=h(r), \qquad r_w\leq r\leq R. \tag{13}$$

The numerical algorithm

In this section, we develop a numerical algorithm for the full problem Eq. 8–13. The weak formulation of this problem is :

$$\text{Find} \quad \phi\in W \quad \text{such that} \qquad a(\phi,v)=f(v), \qquad \forall v\in V \tag{14}$$

where

$$a(\phi,v)=\int_{\Omega(h)} r\nabla\phi\nabla v\, d\Omega, \tag{15}$$

$$f(v)=\int_{z_b}^{z_u} qr_w v dz, \tag{16}$$

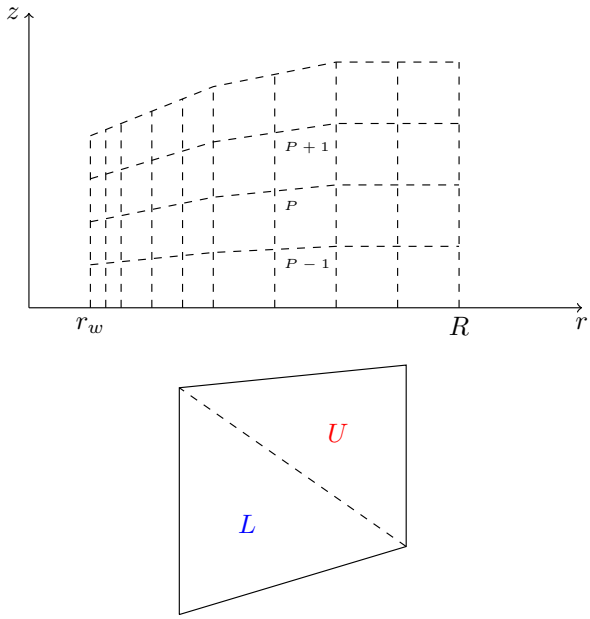

Figure 3: Discretized domain, and one unit consisting of two elements

having

$$V = \{v \in H^1(\Omega(h)) : v|_{r=R} = 0\}, \tag{17}$$

$$W = \{v \in H^1(\Omega(h)) : v|_{r=R} = H_0\}, \tag{18}$$

and $\Omega(h) = \{r, z : 0 \leq z \leq h(r), r_w \leq r \leq R\}$ is defined by the constraint Eq. 13. The problem is solved numerically by a linear finite element method (see e.g. [8]), based on a mesh similar to the one given in Fig. 3. The grid is equidistributed in the z-direction, but we allow for a finer grid in the r-direction near the well.

The discrete variational problem, using $\phi_h = \sum_P \phi_P \varphi_P$ where φ_P are the classical hat base functions becomes

$$\int_{\Omega(\mathbf{h})} \left(\sum_P \phi_P \nabla \varphi_P \right) \nabla \varphi_Q r d\Omega = \int_{z_b}^{z_u} q \varphi_Q \, r dz, \qquad \forall Q \in \mathring{\mathcal{N}} \tag{19}$$

where the sums are over all $P \in \mathcal{N} = \{1, 2, \ldots, N\}$, $\overset{\circ}{\mathcal{N}}$ is the set of gridpoints for which the solutions is not known (excludes the Dirichlet grid points at the right boundary). Let the set of gridpoints for the upper boundary be denoted by P_u and the discrete form of Eq. 13 becomes $\phi_P = h_P, \forall P \in P_u$.

By the standard manipulations, Eq. 19 can be written as

$$\sum_P \left(\int_\Omega \nabla\varphi_Q \cdot \nabla\varphi_P \, r d\Omega \right) \phi_P = \int_{z_b}^{z_u} q\varphi_Q \, r dz, \qquad \forall Q \in \overset{\circ}{\mathcal{N}}. \tag{20}$$

and $\phi_P = h_P, \forall P \in P_u$. We end up with a set of nonlinear equations of the form

$$A(\mathbf{h})\mathbf{\Phi} = \mathbf{f} \tag{21}$$

$$\mathbf{\Phi}_u = \mathbf{h}, \qquad \text{(Upper boundary points)} \tag{22}$$

where A is $\overset{\circ}{N} \times N$ matrix which depends on the gridpoints at the top boundary $\mathbf{h}$, and $\mathbf{\Phi}$ is the vector of the numerical solution in all gridpoints, including the Dirichlet points. The construction of the matrices and the vectors will be explained in the Appendix.

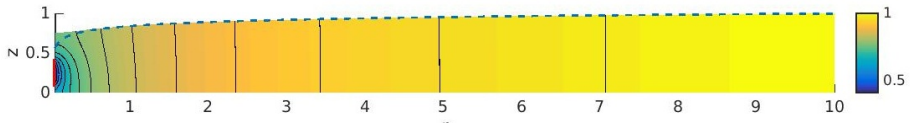

Figure 4: Numerical solution of the full model for $Q = 0.4$. The corresponding Dupuit solution is marked with a dashed line.

3 Numerical test

In this section we will use the above method to find the location of the water table in a steady state flow towards the well based on synthetic data. We also compare the numerical result with the analytical solution which can be calculated by using the Dupuit-Forchheimer assumption. For all numerical and analytical solutions tests we use the geometry $r_w = 0.05, R = 10$ and the well screen is located between $z = 0.1$ and $z = 0.4$. The height of the undisturbed water table at $r = R$ is $H_0 = 1$. We used 40 equally distributed gridponts in the

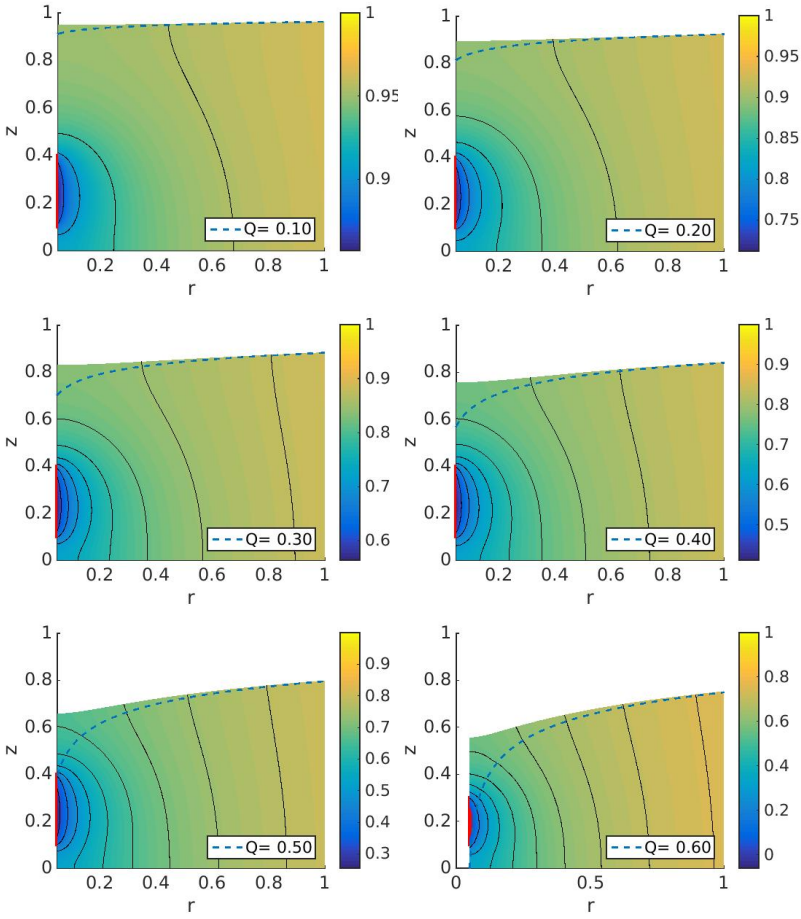

Figure 5: Closeup of numerical and Dupuit solutions of Fig. 4.

z-direction and 200 nonuniformly distributed in the $r-$ direction.

The numerical solution of the piezometric head ϕ and the domain $\Omega(h)$ is presented in Fig. 4, and the location of the water table is compared with the height approximated from the Dupuit-Forchheimer approximation given by Eq. 5 for $Q = 0.4$. We observe that the Dupuit-Forchheimer solution is reasonable

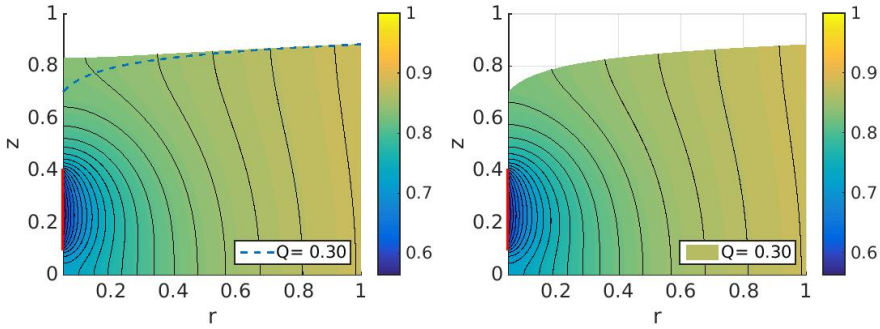

Figure 6: The numerical solutions of the free surface boundary (left) and Dupuit-Forchheimer geometry (right) for $Q = 0.3$.

for $r \gtrsim 1$. The same experiment, with the same geometry, has been conducted for various values of Q, and the results in the region close to the well are given in Fig. 5. As expected the difference between the Dupuit-Forchheimer and the full model solutions increases with increasing Q. We also observe that the water table is perpendicular to the well, indicating no flow of water in the upper left corner. Also, as expected, the equipotential lines are perpendicular to the surface, the flow of water follows the surface. The numerical scheme fails to find a solution for $Q \geq 0.6$.

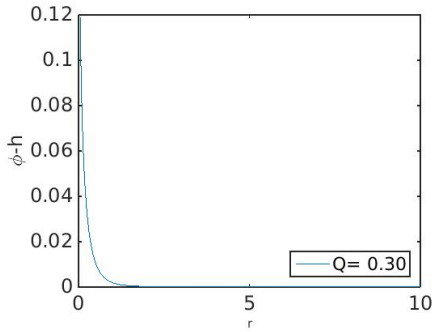

Figure 7: The difference between numerical solutions of the free surface boundary and Dupuit-Forchheimer geometry when $Q = 0.3$.

Finally, we have compared the solution of Eq. 8, both for the geometry given by the full problem, and that of the Dupuit-Forchheimer solutions, for the pumping rate $Q = 0.3$. The results are presented in Fig. 6 and 7.

4 Conclusion

In this preliminary study, we have constructed a scheme for solving groundwater flow equation around a well at steady state. Our numerical scheme has been able to find solutions for very small values of r_w, a situation for which the Dupuit-Forchheimer solution is completely unreasonable since $h(r_w) < 0$. Even if our numerical algorithm works for determining the location of the free surface, this simple study has raised a lot of questions we would like investigate in the future. First of all, we would like to prove existence and uniqueness of the solution of the full problem. We would like to understand why our code fails for large pumping rates.

Bibliography

[1] Bear, J. and Cheng, A. (2008). *Modeling groundwater flow and contaminant transport*, volume 23. Springer Verlag.

[2] Chaiyo, K., Rattanadecho, P., and Chantasiriwan, S. (2011). The method of fundamental solutions for solving free boundary saturated seepage problem. *International Communications in Heat and Mass Transfer*, 38(2):249–254.

[3] Dagan, G., Lessoff, S., and Fiori, A. (2009). Is transmissivity a meaningful property of natural formations? conceptual issues and model development. *Water resources research*, 45(3).

[4] Haitjema, H. (1995). *Analytic element modeling of groundwater flow*. Academic Press.

[5] Kitterød, N.-O. (2004). Dupuit-Forchheimer solutions for radial flow with linearly varying hydraulic conductivity or thickness of aquifer. *Water resources research*, 40(11).

[6] Larabi, A. and De Smedt, F. (1997). Numerical solution of 3-d groundwater flow involving free boundaries by a fixed finite element method. *Journal of hydrology*, 201(1):161–182.

[7] Molson, J., Frind, E., and Palmer, C. (1992). Thermal energy storage in an unconfined aquifer: 2. model development, validation, and application. *Water Resources Research*, 28(10):2857–2867.

[8] Quarteroni, A. (2010). *Numerical models for differential problems*, volume 2. Springer.

[9] Strack, O., Barnes, R., and Verruijt, A. (2006). Vertically integrated flows, discharge potential, and the dupuit-forchheimer approximation. *Groundwater*, 44(1):72–75.

Appendix

Construction of the discretized system

We use linear element functions on a structured grid and the grid is typically be as given in Fig. 8.

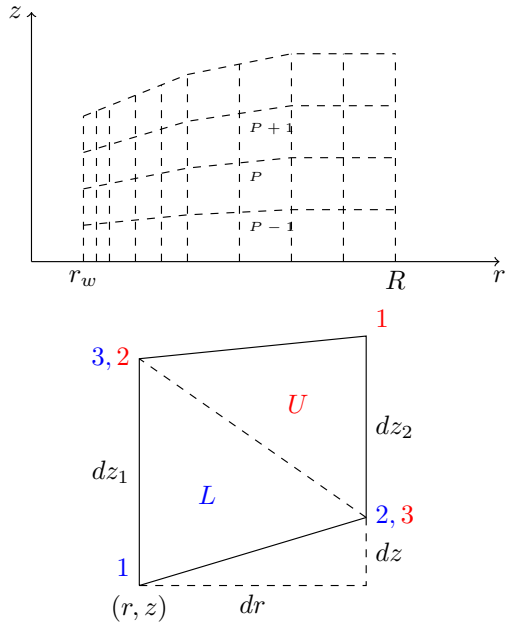

Figure 8: Discretized domain, and one unit consisting of two elements

The gridpoints are

$$r_{i+1} = r_i + dr_i, \qquad z_{i,j+1} = z_{i,j} + dz_{i,j}, \quad i = 1, \ldots, N_r,\ j = 1, 2, \ldots, N_z$$

where

$$r_1 = r_w,\ r_{N_r+1} = R, \quad z_{i,1} = 0,\ z_{i,N_z+1} = Z(r_i).$$

The gridpoints are labelled such that $P = i(Nz + 1) + j$. In the code, we have considered the trapezoidals as a unit, and divided each into an upper and

a lower triangular, as indicated above, each element is labelled by the lower left gridpoint. The local gridpoints for the triangles are indicated by blue (lower triangle) and red (upper triangle).

In the following, we will somewhat ambiguous denote the trapezoidal bounded by the gridpoints $P, P+1, P+N_z+1, P+N_z+2$ as a unit consisting of two triangular elements, and use K as index for this unit, see Fig. 8. However, K corresponds to the index of the lower left corner of the unit, so $K \in \mathcal{K}$, that is the indices of all the gridpoints except those at the upper and at the right boundary.

The local to global mapping $P = \theta\,(K, \alpha)$ becomes

$$\begin{aligned} &\text{Lower triangle:} \quad \theta\,(K,1) = K,\ \theta(K,2) = K + N_z + 1,\ \theta\,(K,3) = K+1, \\ &\text{Upper triangle:} \quad \theta\,(K,1) = K + N_z + 2,\ \theta(K,2) = K+1,\ \theta\,(K,3) = K + N_z. \end{aligned} \tag{23}$$

Mass matrix A :

The elements of the mass matrix, a_{QP} are given by

$$\begin{aligned} a_{QP} &= \int_\Omega r\nabla\varphi_Q \cdot \nabla\varphi_P \, d\Omega = \sum_K \left(\int_{L^K} r\nabla\varphi_Q \cdot \nabla\varphi_P \, d\Omega + \int_{U^K} r\nabla\varphi_Q \cdot \nabla\varphi_P \, d\Omega \right) \\ &= \sum_K \left(a_{\alpha\beta}^{L,K} + a_{\alpha\beta}^{U,K} \right), \end{aligned}$$

where α, β are the corresponding local indices. Using the notation of Fig. 8 we get the following the element matrices:

$$A_L^K = \frac{3r+dr}{6} \begin{pmatrix} \frac{dz_1^2 - 2dz\,dz_1 + dz^2 + dr^2}{dr\,dz_1} & \frac{-dz_1+dz}{dr} & \frac{dz\,dz_1 - dz^2 - dr^2}{dr\,dz_1} \\ \frac{-dz_1+dz}{dr} & \frac{dz_1}{dr} & -\frac{dz}{dr} \\ \frac{dz\,dz_1 - dz^2 - dr^2}{dr\,dz_1} & -\frac{dz}{dr} & \frac{dz^2+dr^2}{dr\,dz_1} \end{pmatrix}$$

$$A_U^K = \frac{3r+2dr}{6} \begin{pmatrix} A_U^K(1,1) & A_U^K(1,2) & A_U^K(1,3) \\ A_U^K(2,1) & A_U^K(2,2) & A_U^K(2,3) \\ A_U^K(3,1) & A_U^K(3,2) & A_U^K(3,3) \end{pmatrix}.$$

where

$$
\begin{aligned}
A_U^K(1,1) =& \frac{dz_1^2 - 2dz_1\,dz + dz^2 + dr^2}{dr^2\,dz_2^2},\\
A_U^K(1,2) =& \frac{-dz_1 + dz}{dr},\\
A_U^K(1,3) =& \frac{-dz_1^2 + 2dz_1\,dz + dz_1\,dz_2 - dz^2 - dz\,dz_2 - dr^2}{dr\,dz_2},\\
A_U^K(2,1) =& \frac{-dz_1 + dz}{dr},\\
A_U^K(2,2) =& \frac{dz_2}{dr},\\
A_U^K(2,3) =& \frac{dz_1 - dz - dz_2}{dr},\\
A_U^K(3,1) =& \frac{-dz_1^2 + 2dz_1\,dz + dz_1\,dz_2 - dz^2 - dz\,dz_2 - dr^2}{dr\,dz_2},\\
A_U^K(3,2) =& \frac{dz_1 - dz - dz_2}{dr},\\
A_U^K(3,3) =& \frac{dz_1^2 - 2dz_1\,dz - 2dz_1\,dz_2 + dz^2 + 2dz\,dz_2 + dz_2^2 + dr^2}{dr\,dz_2}.
\end{aligned}
$$

Assembly of the matrix:

We construct the extended stiffness matrix A_e, including all the elements for all vertices. The elements are stored in a sparse matrix of dimension $N \times N$. The assembly process is illustrated in Fig. 9.

The problematic issue is to put the contributions from the different elements at the right place in A_e. For instance,

$$
\begin{aligned}
a_{PP} &= a_{11}^{L,P} + a_{22}^{U,P-1} + a_{33}^{L,P-1} + a_{11}^{U,P-N_z-2} + a_{22}^{L,P-N_z-1} + a_{33}^{U,P-N_z-1},\\
a_{P,P+N_z+1} &= a_{12}^{L,P} + a_{21}^{U,P-1} \Rightarrow a_{P-Nz-1,P} = a_{12}^{L,P-Nz-1} + a_{21}^{U,P-Nz-2}, \quad P \in \mathcal{K} + N_z + 1\\
a_{P,P-1} &= a_{31}^{L,P-1} + a_{13}^{P,P-N_z-2} \Rightarrow a_{P+1,P} = a_{31}^{L,P} + a_{13}^{U,P-N_z-1,}, \quad P \in \mathcal{K} + 1
\end{aligned}
$$

The element a_{QP} gets a contribution from $a_*^{*,K}$. Make sure P is denotes the column index, solve K with respect to P and you know where to add the contribution.

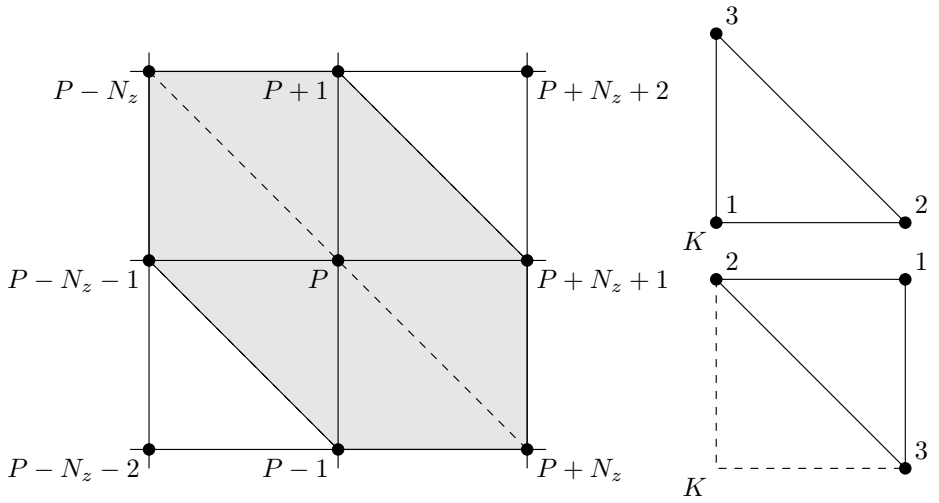

Figure 9: Assembly

Neumann boundary condition

Consider the term

$$\int_{z_b}^{z_u} q\varphi_Q \, r dz, \tag{24}$$

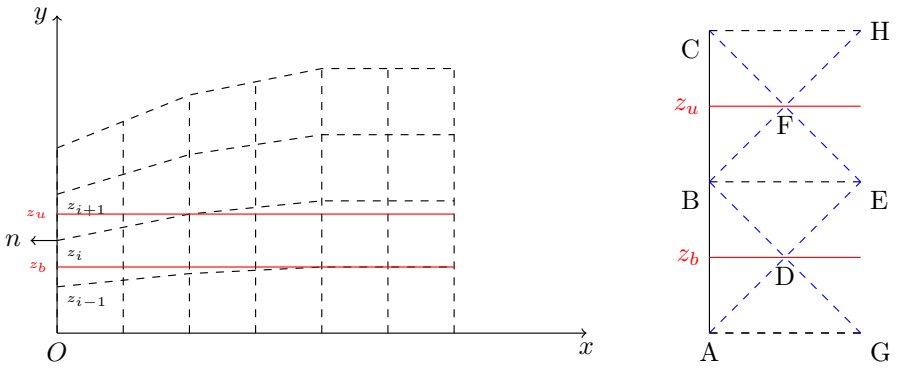

Figure 10: The location of the screen compared to the gridpoints of the well boundary.

in Eq. 20. In our case we have Neumann boundary on the screen of the well $z_b \leq z \leq z_u$. The grid points of our domain may not coincide with the upper and lower location of the well screen. If the two locations coincide with the grid points by the trapezoidal rule we get

$$\int_{z_b}^{z_u} q\varphi_Q \, r dz = r_m \frac{L}{2} q \tag{25}$$

where $r_m = \frac{r_{z_b} + r_{z_u}}{2}$ and L is the length of the edge. If the screen locations not coincide with grid points as shown in Fig. 10 we need to modify the contribution from each edge to the corresponding grid points particularly the upper and lower edge of the screen.